The Dependence of Halo Mass on Galaxy Size at Fixed Stellar Mass Using Weak Lensing

by

Paul Charlton

A thesis
presented to the University of Waterloo
in fulfillment of the
thesis requirement for the degree of
Master of Science
in
Physics

Waterloo, Ontario, Canada, 2017

Author's Declaration

This thesis consists of material all of which I authored or co-authored: see Statement of Contributions included in the thesis. This is a true copy of the thesis, including any required final revisions, as accepted by my examiners.

I understand that my thesis may be made electronically available.

Statement of contributions

The galaxy size fits were performed using code based upon Sumeet Khatri's GALFIT fit processing scripts. The processing and analysis forming the majority of this thesis are my own work.

Abstract

Stellar mass has been shown to correlate with halo mass, but with significant scatter. The stellar mass-size and luminosity-size relationships of galaxies also show significant scatter in galaxy sizes for a fixed stellar mass. Investigating potential links between dark matter halo mass and properties of the baryons, like size, allows us to develop physical explanations for the observed variation in terms of how the baryons and dark matter interact. Galaxy-galaxy lensing allows us to probe the dark matter halos for stacked samples of galaxies, giving us an observational tool for finding halo masses. We extend the analysis of the galaxies in the CFHTLenS catalogue by fitting single Sérsic surface brightness profiles to the lens galaxies in order to recover half-light radius values, allowing us to determine halo masses for lenses according to their size. Comparing our halo masses and sizes to baselines for that stellar mass allows us to do a differential measurement of the halo mass-galaxy size relationship at fixed stellar mass, defined as: $M_h(M_*) \propto r_{\rm eff}^{\eta}(M_*)$, and compare $\eta(M_*)$ over the mass range of our sample. We find that on average, our lens galaxies have an $\eta = 0.42 \pm 0.12$, i.e. larger galaxies live in more massive dark matter haloes. The trend is weakest for low mass blue galaxies and strongest for high mass large red galaxies (LRGs). This suggests that different processes are responsible for the strength of the observed trend over our range of stellar mass bins. Investigation of this relationship in hydrodynamical simulations suggests that this effect is strongest in satellite galaxies, and that the trend we observe in our data should be driven primarily by the fraction of satellite galaxies.

Acknowledgements

I want to thank my M.Sc. supervisors Dr. Mike Hudson and Dr. Michael Balogh for their invaluable assistance, comments, suggestions, guidance, and the always informative conversations we've had over the course of my research. The members of my advisory and defence committees (Drs. Niayesh Afshordi, James Taylor, and Michel Fich) for their feedback and suggestions. I also want to acknowledge my fellow University of Waterloo Astronomy graduate students, to whom I've asked more than my fair share of questions.

Dedication

This thesis is dedicated to my family for their incredible love and support as I've pursued my passion, and the wonderful friends I've made in my studies here.

Table of Contents

List of Figures

List of Tables

List of Abbreviations

AEGIS: All-Wavelength Extended Groth Strip International Survey

CFHT: Canada-France-Hawaii Telescope

CFHTLS: Canada-France-Hawaii Telescope Legacy Survey

CFHTLenS: Canada-Fance-Hawaii Telescope Lensing Survey

HST: Hubble Space Telescope

LRG: Luminous Red Galaxy

NFW: Navarro, Frenk, White

PSF: Point Spread Function

SHMR: Stellar-to-Halo Mass Ratio

SDSS: Sloan Digital Sky Survey

Chapter 1

Introduction

1.1 Galaxy Formation

Understanding how galaxies form and evolve provides a road map we may use to investigate possible specific processes responsible for the halo mass-size relationship. The background for this section is primarily from Mo et al. (2010). We primarily focus on how galaxies form and evolve in such a way as to create a distribution of sizes and halo masses at a given stellar mass. We consider evolution both in the field and in a cluster or group environment, due to the dramatic effects that the cluster environment can have on a galaxy.

The favoured model of galaxy formation and evolution is hierarchical. Primordial density fluctuations in the early universe establish the dark matter-dominated gravitational footprint for the future growth of structure: galaxies, clusters, and voids. In the radiation dominated epoch of the early universe, these perturbations grow very slowly. After the radiation-dominant epoch, matter (both dark and baryonic) then begins to dominate the energy density. Baryons oscillate due to their coupling (via Thompson scattering) to the radiation in the hot baryon-photon plasma of the early universe, but dark matter's lack of interaction with radiation allows it to decouple and begin to collapse, forming the beginnings of structure. Once the universe cools during the era of recombination, the baryonic perturbations are then able to collapse. Thus, the scales of these dark matter and baryonic perturbations are frozen in.

In the matter-dominated universe, the density perturbations begin to collapse due to a lack of pressure support, and grow in amplitude. The overdense perturbations grow into dark matter halos and star-forming gas collects in their gravitational potentials, providing the components for galaxy formation. In these early galaxies, the star-forming gas is heated to the virial temperature ($T_{\rm vir}$), having experienced shock heating as it accretes onto the dark matter halo. Baryonic matter is capable of cooling radiatively, meaning it is capable of forming much more compact structures than dark matter, leading to star formation at the centers of halos. However, not all galaxies have an equal ability to cool. The cooling time depends upon $T_{\rm vir} \propto M^{2/3}$, the virial temperatures of low mass galaxies ($M_{\rm baryon} \lesssim 10^8 M_\odot$) are too low to cool efficiently, and very massive galaxies ($M_{\rm baryon} \gtrsim 10^{12} M_\odot$) cannot cool within the age of the universe. The efficiency of galaxy cooling is described by the cooling curve, which accounts for mass, density, temperature, and metalicity of the gas (Rees & Ostriker 1977; White & Rees 1978; Blumenthal et al. 1984)

Press & Schechter (1974) provides an analytical model for the the number density of halos between mass M and $M + {\rm d}m$ at a given time t:

$$n(M,t){\rm d}M = \frac{\overline{\rho}}{M^2} f_{\rm PS}(\nu) \left| \frac{{\rm d}\ln\nu}{{\rm d}\ln M} \right| {\rm d}M \tag{1.1}$$

Here $\nu = \delta_{\rm c}/\sigma(M)$ is the ratio of the minimum overdensity for structure formation to the RMS of the mass density field established by the early universe fluctuations. $f_{PS} = \sqrt{\frac{2}{\pi}}\nu \exp\left(-\frac{\nu^2}{2}\right)$ gives the fraction of mass in halos over a mass range $\ln\nu$. This theory is broadly successful at describing the abundance of galaxies near the peak of this distribution. However, it slightly overpredicts the number of low and high mass galaxies. Accounting for subhalos (Bond et al. 1991) and mergers (Lacey & Cole 1993) resulted in the Extended Press-Schechter formalism, and the introduction of ellipsoidal collapse of halos (as opposed to spherical collapse assumed previously) improved the accuracy in comparison to simulations further still (Sheth et al. 2001).

1.2 Galaxy Evolution

The process of perturbation expansion, decoupling, and growth in the early universe is fairly deterministic. Given the homogeneity of the early universe, the power spectrum of primordial fluctuations should be responsible for the mass of a resultant galaxy. For the variability we observe, we must now look at how galaxies evolve. Much of this section is based on the results of Behroozi et al. (2013).

1.2.1 Mass Buildup

We are interested in how galaxies grow in both stellar mass and halo mass under the assumption that growth in stellar mass can be related to the apparent size of the galaxy. The gas mass plays a role in determining the mass available for star formation, and its removal by various processes is considered in the next section. The overall efficiency of star formation appears to show a strong dependence on the age of a given galaxy. The higher a galaxy's halo mass at $z = 0$, the earlier its star formation rate (SFR) seems to peak, with some low mass galaxies' star formation rate peaking very recently ($z < 1$) (Behroozi et al. 2013). Interestingly, this coincides with a peak SFR when the galaxy's halo mass is approximately the Milky Way's halo mass. At early times, galaxies more efficiently turn gas into stars, which is likely linked to attributes of the initial formation process.

The collapse that forms galaxies is not simultaneous for all overdensities, as the largest amplitude perturbations collapse first (Gunn & Gott 1972) which leads to different concentrations according to the scale of the universe at the time of collapse. These differing concentrations are one of the first ways that the halo may be linked to galaxy morphology for a fixed stellar mass, as concentration is linked to mass accretion rates (Wechsler et al. 2002). Since the halo is much more massive than the stars one might expect its potential to impact the size of the galaxy that forms by influencing the density of star-forming gas. One reason for this is that the amount of localized star formation within a galaxy is dependent on the density of star-forming gas according to the Kennicutt-Schmidt law (Schmidt 1959; Kennicutt 1998):

$$\Sigma_{\mathrm{SFR}} \propto \Sigma_{\mathrm{gas}}^{n} \tag{1.2}$$

where n is an empirically determined power (≈ 1.4). So in a very compact halo we might expect much denser gas to form more stars.

An important counter to star formation is its suppression by feedback processes. Feedback refers to the injection of energy into gas, which delays or halts the formation of new stars. Low mass galaxies can be quenched by the process of star formation itself. Short-lived high mass stars that end their lives in supernovae are capable of heating gas, and in very low mass galaxies, removing it completely. This is believed to be one process responsible for the low efficiency of star formation in low-mass galaxies, as they are less able to retain the heated gas. If the gas a larger radii is more weakly bound, it should be preferably removed, leaving a smaller galaxy. In very massive galaxies, active galactic nuclei (AGN) play a similar role, and may be responsible for the heating that creates the intracluster medium.

Of course, galaxies do not evolve in isolation. Multiple galaxies may form in close proximity, and if they are not separated by the expansion of the universe they will eventually merge. Mergers and accretion processes should be responsible for the growth of dark matter mass over time, but their role in stellar mass growth is more complicated, depending on both stellar mass and age. For $z > 1$ nearly all galaxies' primary mode of stellar mass growth is through star formation, with only the most massive galaxies growing primarily via mergers. This transition point between quenched and star-forming has transitioned to lower masses over time, with the equivalence point residing at galaxies of the Milky Way's mass today (Behroozi et al. 2013). The merger history of galaxies can vary significantly. In two extreme cases, a galaxy of a given stellar mass may grow through accreting many small satellites with a high ratio of dark matter to baryons, or may experience a single large merger with a galaxy closer to its own mass. Though the galaxies in question may end up with the same mass in stars, their halo masses and morphology are likely to be quite different due to differing amounts of star formation and dark matter accretion.

1.2.2 Mass Removal

The most extreme overdensities form clusters and groups with massive elliptical galaxies near their centers. Groups and clusters have a very high density of galaxies which can be distrupted by nearby galaxies gravitationally. The

radius at which a galaxy's self gravity is balanced by the tidal force exerted by nearby objects is the tidal radius (equation 12.17 of Mo et al. 2010)

$$r_{\rm t} = \left\{ \frac{m/M(<R)}{[3 + m/M(<R)]} \right\}^{\frac{1}{3}} R \tag{1.3}$$

where m is the mass interior to $r_{\rm t}$, $M(<R)$ is the mass of the galaxy exerting the tidal force, and R is their separation. The tidal radius decreases as mass is stripped away, as the mass of the stripping galaxy increases, and as their separation decreases. This tidal stripping process should work from the outside-in; initially the most loosely bound material is removed, primarily the outer dark matter halo, hot gas, and parts of the stellar halo, but over time significant portions of more tightly bound stars may be removed. The end result of this process is essentially accretion of the infalling galaxy's dark matter, with the satellite halo completely added to the group halo, and the stars contributing partially to the intracluster light and partially to the central galaxy's stellar mass.

The denser cluster medium itself is also responsible for removing mass. Ram pressure acts upon a galaxy infalling at speed v according to

$$P = \frac{1}{2}\rho v^2 \tag{1.4}$$

where ρ is the density of the intracluster medium (primarily plasma). This process heats the star-forming gas and removes it from the infalling galaxy, this is one way of rapidly quenching star formation.

1.2.3 Scaling Relations

Galaxy size is understood to have several scaling relationships allowing observers to use it to discern other properties. The fundamental plane (Dressler et al. 1987; Djorgovski & Davis 1987) for elliptical galaxies is one of the most well known of these and relates size r to the surface brightness Σ and velocity dispersion σ. In concert with the redshift to convert apparent size to physical size, these three parameters are enough to discern several intrinsic properties such as mass

$$M \propto \sigma^2 r \tag{1.5}$$

and luminosity

$$L \propto \Sigma r^2 \tag{1.6}$$

which can be combined to determine the mass-to-light ratio.

The more ordered motion of galactic disks allows us to use their Keplerian velocity to determine their mass

$$v_{\rm circ}^2 \propto \frac{M(<r)}{r} \tag{1.7}$$

The Tully-Fisher relation (Tully & Fisher 1977) is a well-known scaling relation for disk galaxies relating their luminosity to their circular velocity. Mo et al. (1998) successfully related the disk properties linked through the Tully-Fisher relation to their dark matter halos. They assumed that the mass and angular momentum of galactic disks are fixed fractions of the mass and angular momentum of their halos. This arises from the formation of the disk following the collapse model of Fall & Efstathiou (1980) in which angular momentum is gained from accreted material given tidal torques at early times. The Tully-Fisher relation can also be used to constrain the distribution of dark matter. Courteau & Rix (1999) found that the residuals of the Tully-Fisher relation using a "submaximal" disk model (dark matter dominates the mass within the disk) correlate only very weakly with the residuals of the size-luminosity relationship, while Dutton et al. (2013) determined that a universal prescription for the interaction of baryons and dark matter is insufficient for the variation in the residuals with galaxy mass.

Galaxy size itself can serve as a cosmological tool. We have already discussed how more stars form where the gas density is higher, in more massive halos. At a fixed redshift, disks are larger than ellipticals for a given mass, and among each type, more massive galaxies are larger, but this relationship evolves; at early times, a galaxy of a given stellar mass is smaller than an equivalently massive galaxy today (e.g. van der Wel et al. 2014). For disk galaxies this size evolution is consistent with with an evolving halo concentration (Somerville et al. 2008; Dutton et al. 2011). For high mass ellipticals, their smaller size at a given redshift may come from stellar buildup in the center, due to dissapative wet mergers (Dekel & Cox 2006; Covington et al. 2008; Dekel et al. 2009). The low mass ellipticals show yet another trend, a flatter mass-size relationship than their high mass counterparts which could point to a different evolution mechanism, such as supernova feedback sup-

pressing star formation(Navarro & White 1993; Gerritsen 1997; Dalla Vecchia & Schaye 2012).

1.3 Objectives

The relationship between baryonic matter and dark matter (DM) remains the source of many open questions in galaxy formation. Studies of the mass-to-light ratio (Faber & Gallagher 1979) and star-to-halo mass ratio (SHMR) of galaxies both show that in general, more massive galaxies tend to live in more massive DM halos. Techniques like abundance matching (Marinoni & Hudson 2002; Kravtsov et al. 2004; Conroy et al. 2006; Vale & Ostriker 2006) show that this relationship is not simply linear or a power law, there is a deficiency of stars in low mass dwarf galaxies and high mass clusters. As well, there is a non-negligible amount of scatter (0.2 dex) in these relationships (e.g. Vale & Ostriker 2006; More et al. 2009; Behroozi et al. 2010;Behroozi et al. 2013; Zu & Mandelbaum 2015) with a currently unknown physical origin. This scatter must have a physical origin so it is useful to search for 2nd order correlations with other parameters of the stellar distribution, such as galaxy size.

Several observational techniques have been used to estimate galaxy halo masses. Dynamical methods are commonly employed, but come with some caveats that limit their usefulness. Using stars as tracers limits one to the region where the baryons dominate, while a full mass measurement requires data out to the virial radius. Using satellites or globular clusters as tracers can improve upon this, but they are not always available. Dynamical mass models usually contain a size dependence, and the mass/light ratio assumed can have considerable impact on the halo properties (Gerhard et al. 2001; Dutton et al. 2005; section 3.3.1 of Courteau et al. 2014). The Tully-Fisher relation and fundamental plane in particular are commonly used in this application. In this thesis we use gravitational lensing to measure halo masses directly at large radii where the halo is dominant over the baryons.

Weak gravitational lensing, particularly galaxy-galaxy lensing (Brainerd et al. 1996; Hudson et al. 1998), is the subtle distortion of background objects due to individual galaxies. It is a combination of the lensing due to baryons, the galaxy's own halo, and any massive haloes the galaxy resides within (i.e.

clusters). It is necessary to stack many similar galaxies to obtain a significant measurement of the halo mass. From this one can infer a mass density distribution, and model the components of the galaxy and halo. This method allows observers to directly determine the average properties of the stacked lenses with considerable precision (Mandelbaum et al. 2006; Velander et al. 2014; Hudson et al. 2015). Previous applications of weak lensing to the study of galaxy evolution have divided galaxies primarily by stellar mass, colour, and redshift. This simple subsampling allows investigation of the broad properties of dark matter as it relates to morphological type and stellar mass, but a more thorough investigation of the physics behind observed scaling relations or scatter as we perform in this thesis requires further subsampling. The large data set that we employ allows me to make the required analysis with weak lensing, without introducing too much statistical uncertainty.

It is reasonable to expect a link between the properties of the dark matter and baryons due to the halo's dominant gravitational role. As an observable, galaxy size has, for example, been linked to the inner regions of elliptical galaxies through the fundamental plane relationship. Recent work has indicated that galaxy size and halo size (a proxy for its mass) are related (Kravtsov 2013; Huang et al. 2017). We also see that size and environment are related, as the results of Bernardi et al. (2007) show, for a given luminosity, brightest cluster galaxies (BCGs) are larger than non-BCGs. The properties of disk galaxies in regards to size are also not fully understood. Using the Tully-Fisher relation (Tully & Fisher 1977) and baryonic Tully-Fisher relation (McGaugh et al. 1999; McGaugh et al. 2000) respectively, Courteau & Rix (1999) and Lelli et al. (2016) both observed that, at a fixed stellar mass, there was little to no size dependence in the rotational velocity, not intuitively expected when considering the role that halo angular momentum should play. Automated surface brightness profile fitting has been shown to provide robust sizes for large samples of galaxies when care is taken to understand and control for the systematics that can influence the fits (Häussler et al. 2007).

In this work, we will assume a power law relationship between galaxy size and halo mass at a fixed stellar mass $M_h(M_*) \propto r(M_*)^\eta$. Determining the value of η is the primary goal of this thesis. We fit this relationship separately for blue (primarily star-forming disk) and red (quiescent elliptical) galaxies in eight mass bins and three redshift bins.

We adopt a flat ΛCDM cosmology, with Hubble parameter $h = 0.7$, matter density parameter $\Omega_{\mathrm{m},0} = 0.3$ and cosmological constant $\Omega_{\Lambda,0} = 0.7$. All relevant quantities are derived using this value of h.

This thesis is organized as follows. In Section 2 we give an overview of the CFHTLenS data used in our analysis. Section 3 describes how we find sizes and halo masses for our lens galaxies, and how we combine them to fit η. We present and discuss our observations in Section 4. To aid in the analysis of our observational results, in Section 5 we compare them with two hydrodynamical simulations. In Section 6 we primarily discuss physical interpretations for the observed η values, the effects that assumptions we make have on our fits. Finally, we summarize our conclusions, and discuss approaches for expanding on our results in Section 7.

Chapter 2

Data and Techniques

2.1 Galaxy-Galaxy Lensing

Gravitational lensing is an observable general relativistic phenomenon caused by the curving of spacetime induced by a massive body, called a lens. Lenses bend the light from background objects, or sources, which leads to their magnification and/or distortion.

Weak lensing is a particular kind of gravitational lensing in which the distortions are very subtle; amounting to minor changes in the shapes of the sources. For the purposes of weak lensing measurements, galaxy shapes are classified by their ellipticity. Ellipticities are quantified by a vector with two components, ϵ_1 and ϵ_2, describing how elongated a circular object is along the x-y axes of an image, and along 45° from the x-y axes, respectively (see Figure 2.1). In the presence of a lens, a source's observed ellipticity $\vec{\epsilon}_{\rm O}$ is not simply its intrinsic ellipticity $\vec{\epsilon}_{\rm I}$, but a combination of the intrinsic ellipticity and the distortion due to the lens:

$$\vec{\epsilon}_{\rm O} = \vec{\epsilon}_{\rm I} + \vec{\gamma} \tag{2.1}$$

where γ is known as the shear.

A source's shear is essentially a transformation of its ellipticity. Rather than describing the shape relative to the image plane, shear describes it relative to the axes formed by a line drawn between the lens and source, and

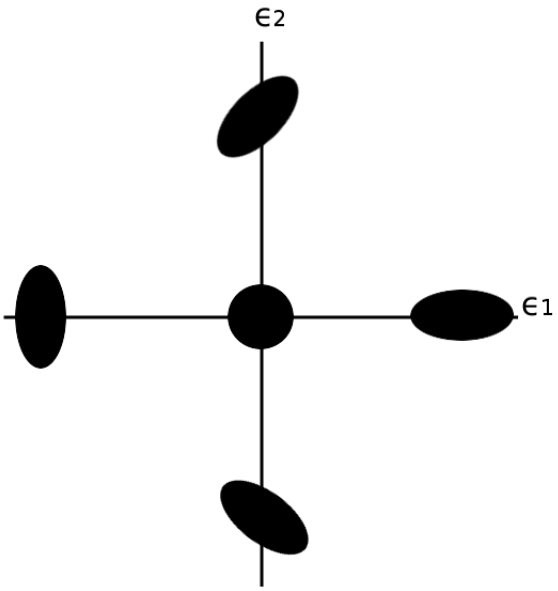

Figure 2.1: The Cartesian plane describing the two ellipticity components of a galaxy's shape.

a line perpendicular. The two shear components are the tangential shear and the cross shear. These are described by

$$\gamma_+ = -\epsilon_1 \cos(2\phi) - \epsilon_2 \sin(2\phi) \tag{2.2}$$

$$\gamma_\times = -\epsilon_1 \sin(2\phi) + \epsilon_2 \cos(2\phi) \tag{2.3}$$

where ϕ is the position angle between the lens and the source (increasing clockwise from the image's horizontal axis). The ellipticities of sources are used to construct their shears which are the quantities required to measure a lensing mass. To do so requires averaging the observed ellipticities of sources, under the assumption that the intrinsic shapes of galaxies are not biased, such that, when averaged, their intrinsic ellipticities equal zero:

$$\langle \vec{\epsilon}_{\rm O} \rangle = 0 + \langle \vec{\gamma} \rangle \tag{2.4}$$

Mass measurements made using weak lensing are statistical in nature. Without the presence of a lens, galaxies have a random distribution of shears. If a lens is present this biases the shears creating an excess of tangential shear.

Cross shear cannot be caused by lensing and should equal zero, but can be caused due to noise in the source shape measurements, and so it is useful for understanding the uncertainties of weak lensing measurements. The mass responsible for the lensing is termed the "excess surface mass density", due to the fact that a uniform "sheet" of mass will not cause any shear, meaning we can only measure the excess:

$$\Delta\Sigma(R) = \overline{\Sigma(< R)} - \overline{\Sigma(R)} \tag{2.5}$$

Miralda-Escude (1991) and Fahlman et al. (1994) related this quantity to the observed tangential shear γ_t through

$$\Delta\Sigma(R) = \Sigma_{\rm crit}\langle\gamma_t(R)\rangle \tag{2.6}$$

which allows us to create a radially averaged distribution of the lensing mass.

The critical density $\Sigma_{\rm crit}$ is defined as follows: starting with the definition of the Einstein radius, at which an Einstein ring forms from a source directly behind a lens:

$$\theta_{\rm E} = \sqrt{\frac{4GM(<\theta_{\rm E})}{c^2}\frac{D_{\rm LS}}{D_{\rm S}D_{\rm L}}} \tag{2.7}$$

where $D_{\rm L}$, $D_{\rm S}$, $D_{\rm LS}$ are the angular diameter distances of the lens, source, and lens-source distance respectively, and $M(<\theta_{\rm E})$ is the mass contained within the Einstein radius. The critical surface density is then

$$\Sigma_{\rm crit} = \frac{M(<\theta_{\rm E})}{\pi\theta_{\rm E}^2} = \frac{c^2}{4\pi G}\frac{D_{\rm s}}{D_{\rm l}D_{\rm ls}} \tag{2.8}$$

Weak lensing requires a minimum signal-to-noise in order to be detectable. In the case of a point mass, this requires a minimum lensing mass, but for a realistically distributed lens, this is a minimum surface density. From van Waerbeke (2000) the error in the lensing mass goes as

$$\Delta M^2 \propto \Sigma_{\rm crit}^2\sigma_\epsilon^2 \tag{2.9}$$

where $\Sigma_{\rm crit}$ is the critical surface density of the lens-source system and σ_ϵ is the scatter of the intrinsic shapes of the sources.

The intrinsic random shape distribution of sources (shape noise) is the primary reason why weak lensing cannot be performed on individual galaxies.

The shear signal is very small, while the shape noise is comparatively large. In order to make this technique useful for objects less massive than clusters, similar galaxies are stacked to reduce the noise. The shape noise error is simply the variance of unlensed galaxy shapes, so its contribution is

$$\sigma_{\rm SN} = \frac{\sigma_\epsilon}{\sqrt{n}} \tag{2.10}$$

where σ_ϵ is the shape noise and n is the number of sources. The total uncertainty in tangential shear measurements is then the sum of the individual measurement errors on the source shapes, and the overall shape noise.

In order to create a mass profile of the lens, the $\gamma_{\rm t}$ are averaged in radial bins. The area covered by a radial band at small distances is much less than at large distances, so n is smaller close to the lens compared to farther away. Light from the lens also interferes with shape measurements for close sources. The precision of shear measurements are reduced very close to the lens, but its primary utility is at large distances where dynamics and other observational methods are limited.

For galaxy-galaxy lensing to provide useful information about halo masses, we must stack galaxies with similar properties. Using stellar mass as the stacking parameter for lenses has provided observational verification for the inefficiency of star formation in very high mass and low mass haloes. This has brought forth gas heating due to supernovae (low mass) and active galactic nuclei (high mass) as an explanation for what is observed. A second useful parameter for stacking is type, disk or elliptical, which can be accomplished by colour, or if morphological information is available, shape. This often splits galaxies by whether they are star-forming or quiescent. We may then separating galaxies by redshift to track evolution over time. The above method has been employed to show that, from $z = 1$ halo masses show significant evolution in elliptical galaxies, with older halos being more massive, while disk galaxies' halo masses remain relatively stable (Hudson et al. 2015). Finally, in concert with simulations, environmental effects can be investigated using the density of galaxies in a given area. Statistically, a larger fraction of galaxies in a high density environment will be satellite galaxies, and subject to tidal stripping. Observations of galaxies at a fixed stellar mass show that, indeed, galaxies in high density environments have less massive halos (Gillis et al. 2013). Photometrically-determined properties are the simplest

to investigate. Information requiring spectra are currently unavailable for a majority of lenses due to the greater time and effort required to obtain them.

2.2 Surface Brightness Profile

Measuring a galaxy's size is not a simple task; in fact, even the definition of size is not clear a priori. The stellar distribution of a galaxy does not simply truncate at a given radius; disk galaxies and ellipticals both have a stellar halo that contributes to the observed starlight, but disks are more well defined. To address these issues, surface brightness profiles allow us to examine the total light distribution of a galaxy and assign it a meaningful size. A commonly used definition that we adopt here is the half-light, or "effective" radius, the radius within which half of the total integrated galactic light is contained.

In order to determine a half-light radius, we must select a surface brightness profile to fit. Disk galaxies are observed to have an exponential profile (Freeman 1970a; Freeman 1970b):

$$\Sigma(r) = \Sigma_0 \exp\left(-\frac{r}{r_\mathrm{s}}\right) \tag{2.11}$$

in which Σ_0 is the central surface brightness and r_s is related to the half-light radius $r_\mathrm{eff} = 1.678 r_\mathrm{s}$. This light profile is centrally concentrated and flat, and decreases significantly at the scale radius, consistent with a disk.

The exponential profile does not contain enough light in the "wings" to effectively fit elliptical galaxies. The de Vaucouleurs profile (de Vaucouleurs 1948) was developed through observations of elliptical galaxies and is a commonly employed surface brightness profile for these galaxies:

$$\Sigma(r) = \Sigma_\mathrm{eff} \exp\left\{-7.67\left[\left(\frac{r}{r_\mathrm{eff}}\right)^{\frac{1}{4}} - 1\right]\right\} \tag{2.12}$$

where Σ_eff is the surface brightness at the effective radius r_eff

While the above profiles fit are useful for the prototypical spiral and elliptical galaxies, many are a mixture, with significant bulge *and* disk components. In these cases it is useful to have an adaptable surface brightness

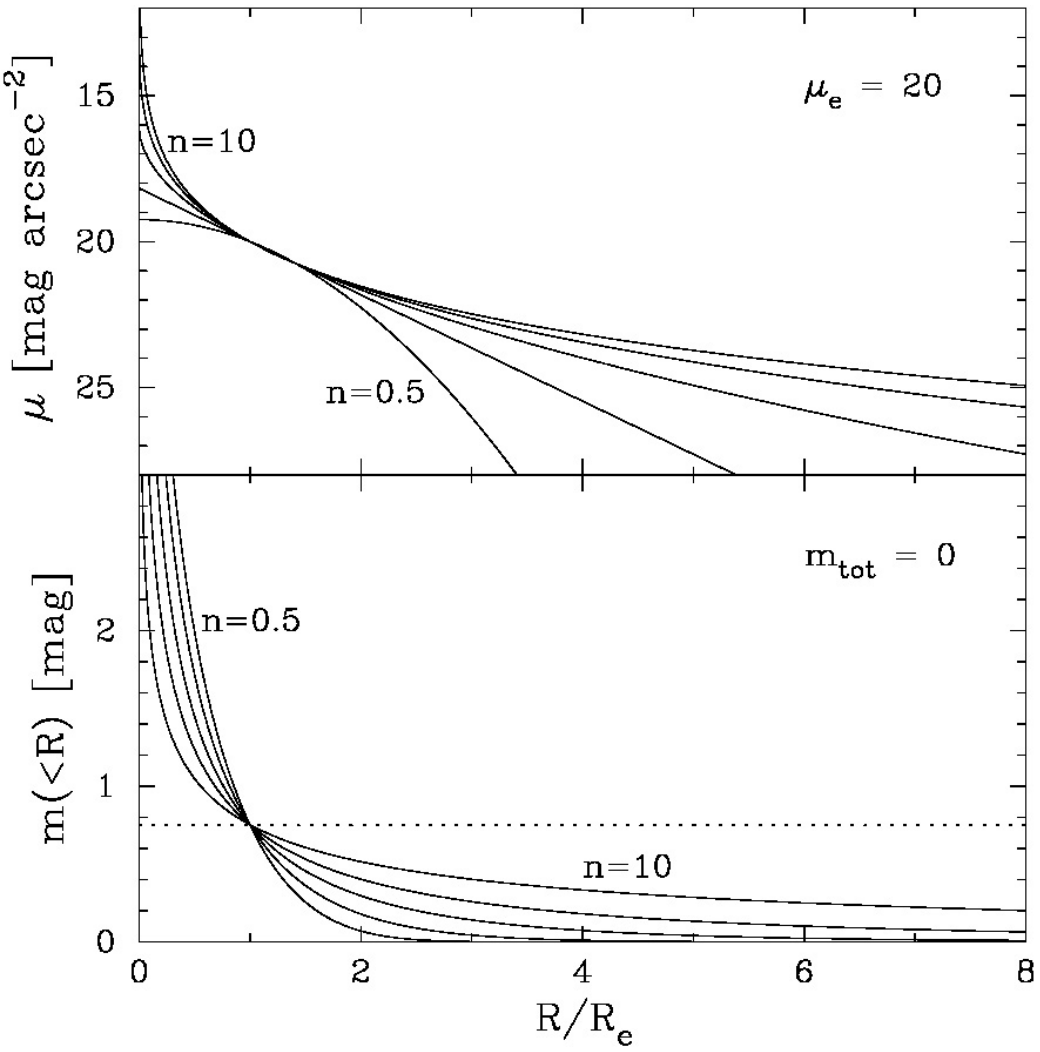

Figure 2.2: Sérsic profile normalized for total surface brightness (top) and total integrated magnitude (bottom) from Graham & Driver (2005). Notice that, when normalized, $r_{\rm eff}$ lies at the same location for all values of n.

profile that can fit the two main types and those in between. For this purpose we use the Sérsic (1963) profile:

$$\Sigma(r) = \Sigma_{\text{eff}} \exp\left\{\kappa\left[\left(\frac{r}{r_{\text{eff}}}\right)^{\frac{1}{n}} - 1\right]\right\} \tag{2.13}$$

This profile is adaptable through changing the Sérsic index n and κ which is fixed by n as described in Ciotti (1991). A low n creates a centrally concentrated profile consistent with disks, while a higher n creates an extended profile consistent with elliptical galaxies.

2.2.1 Profile Fit Optimization

Once the desired profile is selected, it must be fit to an observed galaxy in order to recover a size. We use a least-squares minimization method to compute a reduced χ^2 as our goodness-of-fit indicator

$$\chi^2_\nu = \frac{1}{N_{\text{DOF}}} \sum_{x=1}^{n_x} \sum_{y=1}^{n_y} \frac{(f_{\text{data}}(x,y) - f_{\text{model}}(x,y))^2}{\sigma(x,y)^2} \tag{2.14}$$

Where the summed difference between all pixels of the original image and the model image is minimized by altering parameters of the Sérsic profile until no improvements are made. The complexity of the model is a free choice, for example, a precise method may use two Sérsic profiles, one for the bulge, and one for the disk, but by introducing more free parameters, we increase the time taken to optimize the model and, in this case, the definition of size becomes less clear.

Rough parameter estimates based on galaxy catalogues provide a starting point for our surface brightness fits. Of course, the profiles must be optimized as discussed above using an appropriate algorithm. A complete approach would use a Markov Chain Monte Carlo (MCMC) method such as Metropolis-Hastings in order to explore the entire parameter space, which improves the chance of finding a global best-fit, and provide realistic uncertainties on each parameter fit. However, the MCMC approach can be time-consuming with many-parameter fits if the χ^2 space has many local minima. Instead, the

software we use employs a damped least-squares optimization method. In this method, $f_{\rm model}$ in Equation 2.14 is iterated upon using

$$f_{\rm model}(x_n, \vec{p} + \vec{\delta})_{i+1} \approx f_{\rm model}(x_n, \vec{p})_i) + \vec{\delta}\frac{\partial f_{\rm model}(x_n, \vec{p})_i}{\partial \vec{p}} \tag{2.15}$$

where x_n are the n pixels being fit, $\vec{p}$ is the vector containing the Sérsic + sky fit parameters, and $\vec{\delta}$ is the incrementation of each parameter. $\vec{\delta}$ is determined by using the Jacobian $\mathbf{J}$ and the damping parameter λ, solving the system of equations

$$(\mathbf{J}^T\mathbf{J} + \lambda\mathbf{I})\vec{\delta} = \mathbf{J}(\vec{f}_{\rm data} - \vec{f}_{\rm model}(\vec{p})) \tag{2.16}$$

where $\mathbf{I}$ is the identity matrix. The purpose of the damping parameter is to ensure that χ^2_ν decreases sufficiently. If this does not occur, λ is increased, if it does, λ is decreased. This allows the algorithm to find the true minimization point. The main weakness of this algorithm is that the initial model parameters must be close to the final parameters to guarantee a good fit.

2.3 Imaging and photometry

The data used in this paper are from the CFHT Lensing Survey (CFHTLenS) (Heymans et al. 2012) analysis of the "Wide" portion of the CFHT Legacy Survey (CFHTLS). The imaging data used are comprised of the co-added science images described in Erben et al. (2013). We use the CFHTLenS catalogues of photometric redshifts, luminosities and colours to sort our lens galaxies into bins, and fit surface brightness profiles to divide them into size bins. The catalogues also include shape measurements we use for galaxies photometrically defined as sources in our weak lensing analysis.

The CFHTLenS analysis is performed on the four CFHTLS wide fields (W1 through W4), imaging 154 square degrees. Imaging was performed in five bands, $u*$, g', r', i', z' to a magnitude limit of $i'_{AB} = 24.7$ using the MegaCam/MegaPrime wide-field imaging facility at the Canada France Hawaii Telescope (CFHT).

2.4 Source galaxy ellipticities

We use the source galaxy ellipticities provided by CFHTLenS for 8.7×10^6 background source galaxies (Miller et al. 2013). The source ellipticities have a Gaussian distribution with a scatter of $\sigma_e = 0.28$ (Heymans et al. 2013). The uncertainty induced by this scatter is called the "shape noise". The source ellipticities are used as estimators for the gravitational shear induced by the lens, and when stacked allow for measurements of the average dark matter halo mass. The small additive correction to the source shapes applied in Heymans et al. (2012) and the multiplicative correction of Miller et al. (2013) are ignored here, as the statistical errors in our binned subsamples dominate over any small corrections.

2.5 Redshifts and stellar masses

Redshifts of lenses and sources in CFHTLenS, z_p, are determined photometrically as described in Hildebrandt et al. (2012). The typical error in redshift increases from ± 0.048 for the closest lenses at $z_p = 0.2$ to ± 0.092 for the furthest sources at $z_p = 1.3$.

The redshifts determined above are used to measure the stellar masses. The LePhare code, developed by Ilbert et al. (2006) fits models of star formation history and dust extinction using the $u^* g' r' i' z'$ apparent magnitudes to find stellar masses and rest frame absolute magnitudes. Velander et al. (2014) describes in detail how the models of Bruzual & Charlot (2003) are used for these purposes. The spectral energy distribution templates used to fit the masses assume a Chabrier (2003) initial mass function, and exponentially decreasing star formation rates $\propto e^{-t/\tau}$ with nine different values for τ and two metalicities.

Chapter 3

Methods and Measurements

3.1 Samples

Our sample consists of galaxies categorized as lenses or sources. The lenses are galaxies that we measure sizes for and stack to determine halo masses. For a given lens, the sources are background galaxies with lensing shape measurements that are averaged in radial bins and stacked. Lenses and sources are not mutually exclusive. The criteria outlined below permit a galaxy to be used as both a lens and a source in a stack, should they be met.

3.1.1 Lens galaxy sample

Our lens sample consists of 2.06×10^6 galaxies with $i' < 23$, and $0.2 < z_p < 0.8$ from the CFHTLenS catalogues created with Source Extractor (SExtractor) running on the co-added science images. They are separated into red and blue samples based on their dust-corrected, rest frame $u^* - r'$ colours, dividing them at a value of 1.6, the location of the "green valley" of our lens sample. The redshift range is divided into three groups to account for possible evolution: $0.2 < z_p \leq 0.4$, $0.4 < z_p \leq 0.6$, and $0.6 < z_p \leq 0.8$.

We expect that η may vary as a function of M_* and by galaxy type, as different physical processes are relevant in low mass blue irregulars versus massive central cluster galaxies, for example. To account for this, we divide

our lens sample into eight subsamples with different stellar masses. While we have stellar masses for individual galaxies, they are noisy, and using them to bin would introduce significant Eddington bias due to the slope of the mass function. Instead, we use the r'-band luminosities (which are less noisy and accordingly suffer from less bias) to place galaxies in bins such that when an appropriate stellar mass-to-light ratio is applied, the bins have a 0.5 dex separation in M_*.

3.1.2 Source galaxy sample

The source sample consists of 5.6×10^6 galaxies with $i' < 24.7$ and $z_p < 1.3$, the upper limit for reliable photo-z measurements in CFHTLenS. Galaxies may be used as both a lens or source as required if the criteria for a valid lens-source pair (below) is fulfilled. The magnification due to weak lensing is small, individually, and should have no measurable effect on the fitted galaxy size for lenses.

3.1.3 Lens-source pairs

The average redshift error for galaxies in the middle of our redshift range $z_p = 0.5$ is approximately 0.05. Therefore we select sources with a redshift separation $\Delta z_p > 0.1$, giving a 2σ buffer between pairs.

3.2 Sizes of Lens Galaxies

In order to recover sizes for the lens galaxies in our sample, we use GALFITM (Bamford et al. in prep), a modification of GALFIT3 by Peng et al. (2002, 2010). A postage-stamp cutout is created of each galaxy we wish to fit, with the dimensions determined by equations (2) and (3) in Häussler et al. (2007). The cutout size must be large enough to include as much of the light from the galaxy as possible, and to fit the sky background correctly. Larger cutouts also provide more sky pixels which can improve the fit, but the size must be limited to avoid the inclusion of too many contaminating stars and galaxies which must be masked out.

We fit a single Sérsic profile

$$\Sigma = \Sigma_{\rm e} \exp\left[\kappa((r/r_{\rm e})^{\frac{1}{n}} - 1)\right] \tag{3.1}$$

to the galaxies in the CFHTLenS catalogue and fit a 2D gradient sky background. GALFIT provides several options for light profiles, including double (bulge+disk) Sérsic fits. However since a significant number of the lenses are only just resolved, so we prefer a more robust single Sérsic profile. Due to the number of galaxies fit we do not incorporate any deblending or simultaneous fitting for closely grouped galaxies. Handling of fits affected by this is discussed below.

The large number of galaxies we wish to fit and our computation time limits mean that we cannot deal with poor fits on an individual basis; we instead attempt to minimize the amount of fits that fail. A failed fit occurs when GALFITM crashes (very rare) or reaches its iteration limit with a flagged fit. Flagged fits contain parameters that are unlikely to be physical or reliable, such as an effective radius much smaller than a pixel, or very large Sérsic indexes. Considerable time was spent attempting to reduce the number of failed fits with GALFIT3, with most serious cases of failure being galaxies fit with unphysically small half-light radii. Investgation into these fits showed that most were becoming trapped in local χ^2 minimums near bad values due to large initial steps in parameter space. GALFIT3 does not allow parameters to leave flagged regions (i.e. hard-coded or user-defined limits for a parameter) if the χ^2 value does not improve, GALFITM solves this problem by reverting to the previous good state if a step would lead to a flagged parameter. This switch reduced the fraction of flagged galaxies from $>10\%$ to $<1\%$. The remaining flagged galaxies are not included in stacks, as their recovered sizes are unlikely to be reliable.

3.3 Comparison with AEGIS

In order to provide a more objective check on the quality of our galaxy fits it is useful to compare similar fits to the same galaxies based on higher resolution space-based imaging. The AEGIS survey (Davis et al. 2007) has imaged and catalogued many galaxies in the region around the Extended Groth Strip (EGS) using the Hubble Space Telescope, and Griffith et al. (2012) has fit

Sérsic profiles to these AEGIS galaxies using GALFIT. The AEGIS region lies within four fields of the CFHTLS W3 patch. The primary differences between the two data sets are the PSF size (ACS: 0.1", Megacam: varies 0.5"-1.0") and the lack of a sky background in the fits to HST imaging.

Our lensing analysis is limited to lenses in the range of $0.2 < z_p < 0.8$ and $i' < 23$. We thus have approximately 3800 galaxies in the region covered by AEGIS for comparison. Since we expect there to be some scatter in the fitted model parameters on a per-galaxy basis, we can examine the scatter for trends in magnitude and size to examine where problematic galaxies are. GALFIT convolves the Sérsic profile with a provided PSF in fitting each galaxy, but suggests that unresolved sources ($r_{\rm eff} < 0.5$ pixels) may be better fit with only the PSF. If many small galaxies have their sizes artificially increased, it would increase the median $r_{\rm eff}$ of the low-size bin used to fit η. This would reduce the $\Delta r_{\rm eff}$ without reducing $\Delta M_{\rm h}$, leading to a larger value of η than with unaffected galaxies.

The median fitted size of galaxies from CFHT is less than 0.2% greater, on average, than ACS, while the fitted magnitudes are less than 0.02 brighter, indicating generally good agreement between Sérsic profile fits, and thus $r_{\rm eff}$ for our ground-based imaging. The scatter in the Sérsic index, $r_{\rm eff}$, and apparent magnitude fits between CFHT and ACS increases at fainter magnitudes. Overall, there is a tendency for CFHT fits to have lower Sérsic indexes ($\sim 10\%$ smaller) than the ACS fits. However this is not matched by an offset in magnitude, so while the shape of the surface brightness profile will be slightly impacted, the value of $r_{\rm eff}$ will not. The enlarging effect of atmospheric seeing is not significant. The only galaxies that have a significant systematic disagreement with AEGIS are so small as to be misidentified as stars by CFHT, preventing their inclusion in our sample. Detailed fit comparisons are included in Appendix A.

3.3.1 Purity of the CFHTLenS Galaxy Sample

Our initial galaxy sample consists of objects photometrically identified as galaxies from the CFHTLenS imaging in the SExtractor-created CFHTLenS catalogues; the final sample consists of objects from the initial sample that are successfully fit with an unflagged Sérsic profile. It is critical to minimize the contamination from stars in our galaxy samples because the stars have

Table 3.1: Number of EGS objects classified as galaxies or stars by SExtractor for CFHTLenS and AEGIS. Objects included in the final analysis are shown in bold.

	Unflagged (3159)		Flagged (630)	
	CFHT Galaxy	CFHT Star	CFHT Galaxy	CFHT Star
ACS Galaxy	**3037**	59	117	17
ACS Star	**9**	54	12	479

no lensing signal, and their inclusion in the averaging will reduce the excess surface density signal, thus leading to a lower halo mass when fitted. The AEGIS catalogues include their own star/galaxy classification based on HST observations with much better resolution which allows us to compare the relative ability to classify objects, with specific attention paid to objects classified differently by the two catalogues. The CFHTLS sample will not include galaxies that are misclassified by CFHT as stars, but retain stars misclassified by CFHT as galaxies.

We assume that for the ~ 3800 objects included in both catalogues that the AEGIS classifications, being determined via space-based imaging, are correct. We allow GalfitM to attempt to fit a Sérsic profile to all objects including stars. As shown in Table 3.1 GalfitM flags the fits of most stars, with only 9 out of the 3046 unflagged CFHT-classified galaxies being stars misidentified as galaxies. If we take this sample to be representative, then the expected stellar contamination is approximately 0.3%. The systematic error due to this is small compared to the random errors.

3.3.2 Completeness of galaxy sample

As shown in Table 3.1 (see appendix A for more information), there is some disagreement in star-galaxy separation for some objects in the AEGIS and CFHTLenS data sets, particularly at small apparent sizes where seeing heavily influences the resolution of CFHT imaging. The degree of disagreement in classification is shown in figure 3.1. As the apparent size decreases, more galaxies begin to be incorrectly classified as stars, with 50% of galaxies smaller than $0.15''$ being lost. The loss of small galaxies would shift the

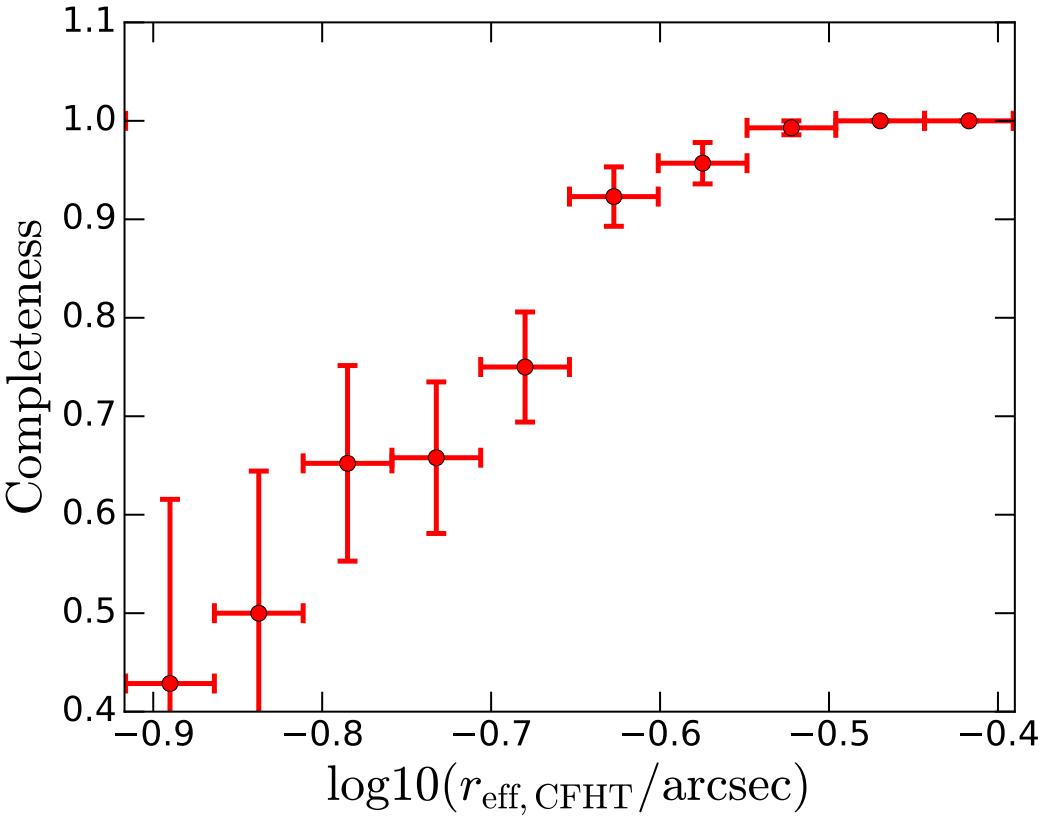

Figure 3.1: Completeness in bins of apparent size as determined from CFHT data. A value of 1 means that 100% objects photometrically identified as galaxies by AEGIS are being identified as galaxies by CFHTLenS. A completeness of 0.5 means that 50% of AEGIS galaxies are being identified correctly by CFHTLenS, with the remaining 50% being misidentified as stars and not included in the final sample.

median galaxy size in all size subsamples to larger values. However, because since our η measurement is differential this amounts to a reduction in dynamic range.

3.4 Halo mass-size dependence η

We wish to make a differential measurement of the relationship between size and halo mass for a fixed luminosity, colour, and redshift bin. We assume a power-law relationship between halo mass $M_{\rm h}$ and half-light radius $r_{\rm eff}$ at fixed M_* of the form:

$$M_{\rm h}(M_*) \propto r_{\rm eff}^{\eta}(M_*) \tag{3.2}$$

In order to compare the relative strength of this relationship across all mass/luminosity bins, we compare M_h and $r_{\rm eff}$ to fiducial masses and sizes for that stellar mass bin. For our fiducial mass, we use the expected stellar mass-to-halo mass ratio (SHMR) for a given M_* (appendix C of Hudson et al. 2015). Our fiducial size is the median size of galaxies of a given M_* from our fits. To account for differences between the expected halo mass of our average sized galaxies and observed galaxies we include a numerical factor A. Note that these expected masses are derived for central galaxies only, they allow us to make the differential mass measurements we require, but we do not expect them to match the average mass of stacked lenses which includes both central galaxies and satellites (i.e. A may not necessarily equal 1):

$$\frac{\langle M_{\rm h}\rangle}{M_{\rm h,exp}(M_*)} = A\left(\frac{r'_{\rm eff,med}}{r_{\rm eff,med}(M_*)}\right)^{\eta} \tag{3.3}$$

Since we stack our lenses, we use $\langle M_{\rm h}\rangle$ and $r'_{\rm eff}$, which, respectively, are the ensemble average halo mass, and the median size of the lenses in each stack.

We perform our analysis in $\log - \log$ space, so for simplicity, we introduce

$$\Delta r'_{\rm eff}(M_*) = \log_{10}\left(\frac{r'_{\rm eff}}{r_{\rm eff,med}(M_*)}\right) \tag{3.4}$$

and

$$\Delta M'_{\rm h}(M_*) = \log_{10}\left(\frac{\langle M_{\rm h}\rangle}{M_{\rm h,exp}(M_*)}\right) \tag{3.5}$$

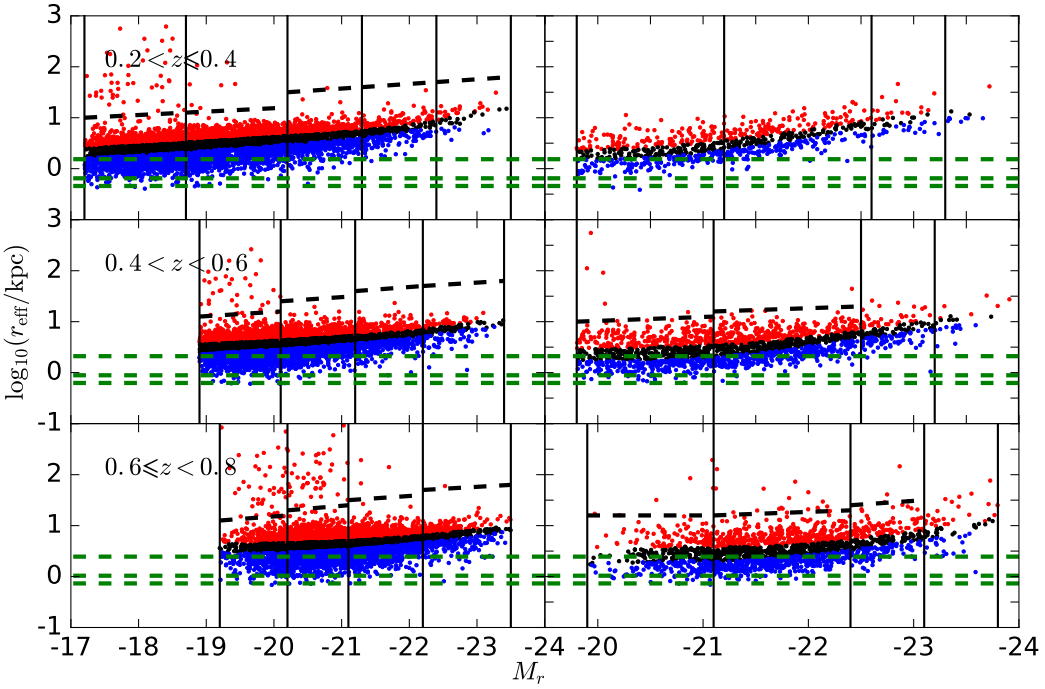

Figure 3.2: Luminosity-size relationship for a random subsample of the fitted blue (left) and red (right) lenses. Points are colour-coded red, black, and blue to denote their inclusion in the large, medium, and small stacks, respectively. The solid black lines mark the boundaries of each luminosity (or average stellar mass) bin. Galaxies larger than the dashed black lines are removed from the stacks, as they are unphysically large and usually the result of a poorly masked secondary object. The dashed green lines, from top to bottom indicate boundary of the 100%, 50%, and 0% completeness regions (section 3.3.2).

Figure 3.2 shows our $r_{\rm eff}$ vs L relationship and demonstrates how we adaptively split our galaxies into small, average and large size bins for their mass. Galaxies that have extremely large $r_{\rm eff}$ are likely to have been poorly fit due to inadequately masked bright companions, bright sky background, etc... These galaxies are removed and the lenses in each size bin are stacked and fitted with a halo model as described in section 3.5.

3.5 Halo masses of lens galaxies

We determine the average dark matter halo mass for galaxies in each of our three size subsamples at a fixed stellar mass. This cannot be done on an individual basis due to measurement and statistical errors so we must first stack the measured tangential shears for each lens source pair as a function of radius. These stacked shears are then used to fit a dark matter profile, giving us the mass we require for our analysis.

3.5.1 Average shear

To determine halo masses from weak lensing, we need to determine the excess surface mass density

$$\Delta\Sigma(R) = \overline{\Sigma(<R)} - \overline{\Sigma(R)} \tag{3.6}$$

which is the difference between the projected average surface mass within a circle of radius R and the surface density at that radius. The tangential shear γ_t can be estimated by averaging the ellipticities of background source galaxies along an axis that is perpendicular to a line connecting the lens and and that source. This tangential shear is directly related to the excess surface density through the equation

$$\Delta\Sigma(R) = \Sigma_{\rm crit}\langle\gamma_t(R)\rangle \tag{3.7}$$

where $\Sigma_{\rm crit}$ is the critical surface density, used to define the Einstein radius of the lens. It is given by

$$\Sigma_{\rm crit} = \frac{c^2}{4\pi G}\frac{D_{\rm s}}{D_{\rm l}D_{\rm ls}} \tag{3.8}$$

where $D_{\rm s}$, $D_{\rm l}$, and $D_{\rm ls}$ are the angular diameter distances to the source, lens, and lens-source distance respectively.

The shape noise is combined with the measurement error on the ellipticities within *lens*fit to give a weight w which is applied when stacking (described in Miller et al. 2013). Each pair is also weighted by $W = \Sigma_{\rm crit}^{-2}$ following Hudson et al. (2015). When stacked, the average excess surface density of our lenses is

$$\langle \Delta\Sigma(R) \rangle = \frac{\sum w_j \gamma_{t,j} \Sigma_{{\rm crit},ij} W_{ij}}{\sum w_j W_{ij}} \tag{3.9}$$

which is summed over all lenses i, and sources j in a given radial bin.

3.5.2 Halo Model

The data are fit with a simplified version of the halo model described in Section 3 of Hudson et al. (2015). We focus on the one-halo term of this model, describing the contribution from the stacked lenses' own stars and dark matter. We model $\Delta\Sigma(R)$ far from the stars, so we can treat the stellar mass as a point mass:

$$\Delta\Sigma_*(R) = \frac{\langle M_* \rangle}{\pi R^2} \tag{3.10}$$

The dark matter halo is modeled by an NFW (Navarro et al. 1997) density profile and is parameterized by its virial mass M_{200}. The halo's concentration c_{200}, and thus scale radius r_s, is fixed by its redshift z and M_{200} using the relaxed halo model from Muñoz-Cuartas et al. (2011). The projected halo surface mass excess term $\Delta\Sigma_{\rm NFW}$ is described in Brainerd et al. (1996) & Bartelmann (1996). The full simplified one-halo term is:

$$\Delta\Sigma_{\rm 1h}(R) = \Delta\Sigma_{\rm NFW}(R) + \Delta\Sigma_*(R) \tag{3.11}$$

Unlike in Hudson et al. (2015) we do not fit the offset group halo term. This term is a convolution of all of the central haloes that satellite lenses are embedded in. The offset group halo term dominates at intermediate radii, outside of the region in which the one-halo term is relevant. Correctly fitting

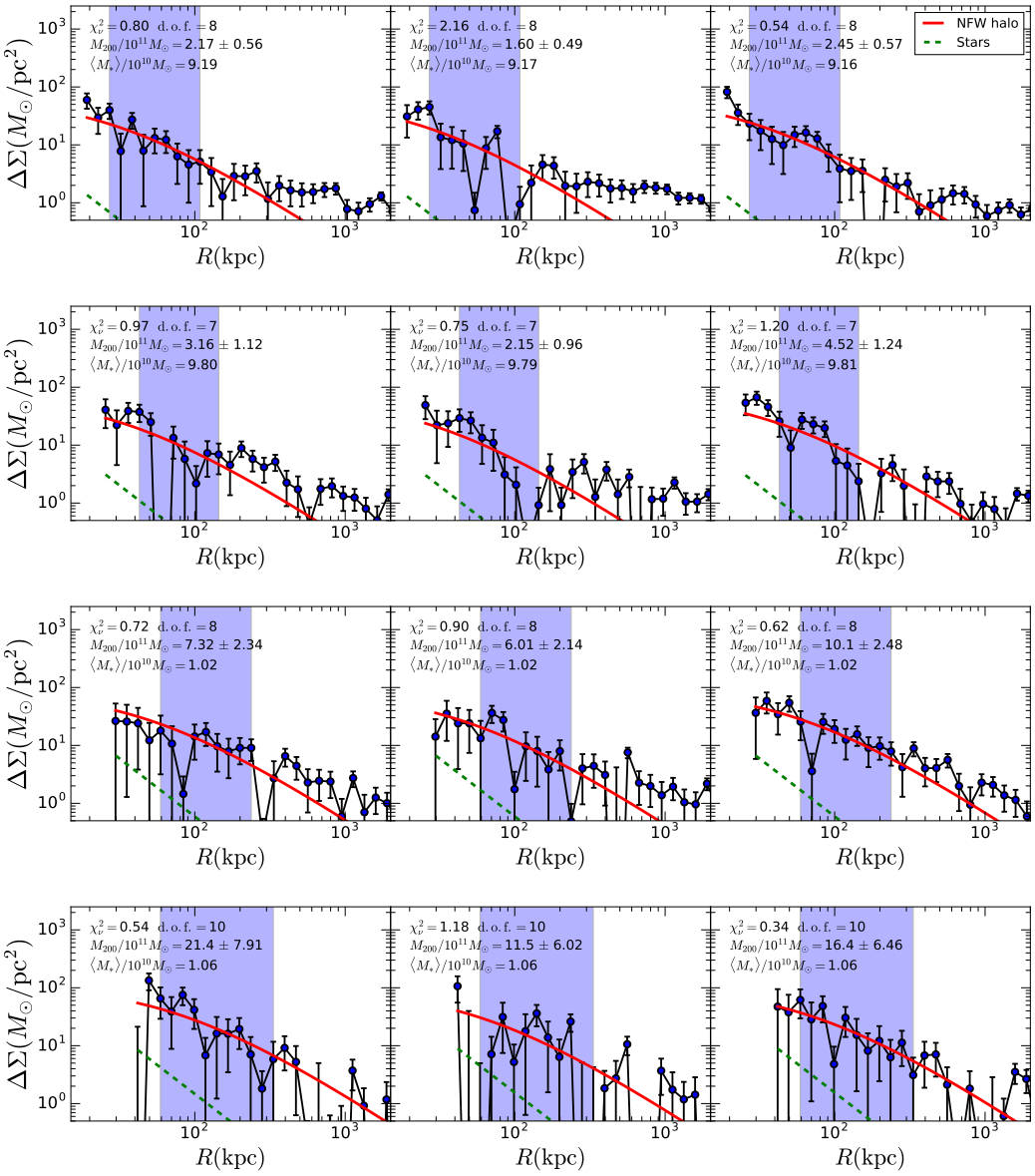

Figure 3.3: Stacked $\Delta\Sigma$ data from CFHTLenS blue galaxies, $0.2 < z < 0.4$, in three size bins, from left to right: small, average, and large. The blue shaded region contains the points used for the one-halo NFW fit, according to Section 3.5.2. The solid red line is the one-halo NFW term and the green dashed line is the stellar component. The average lens mass increases from top to bottom

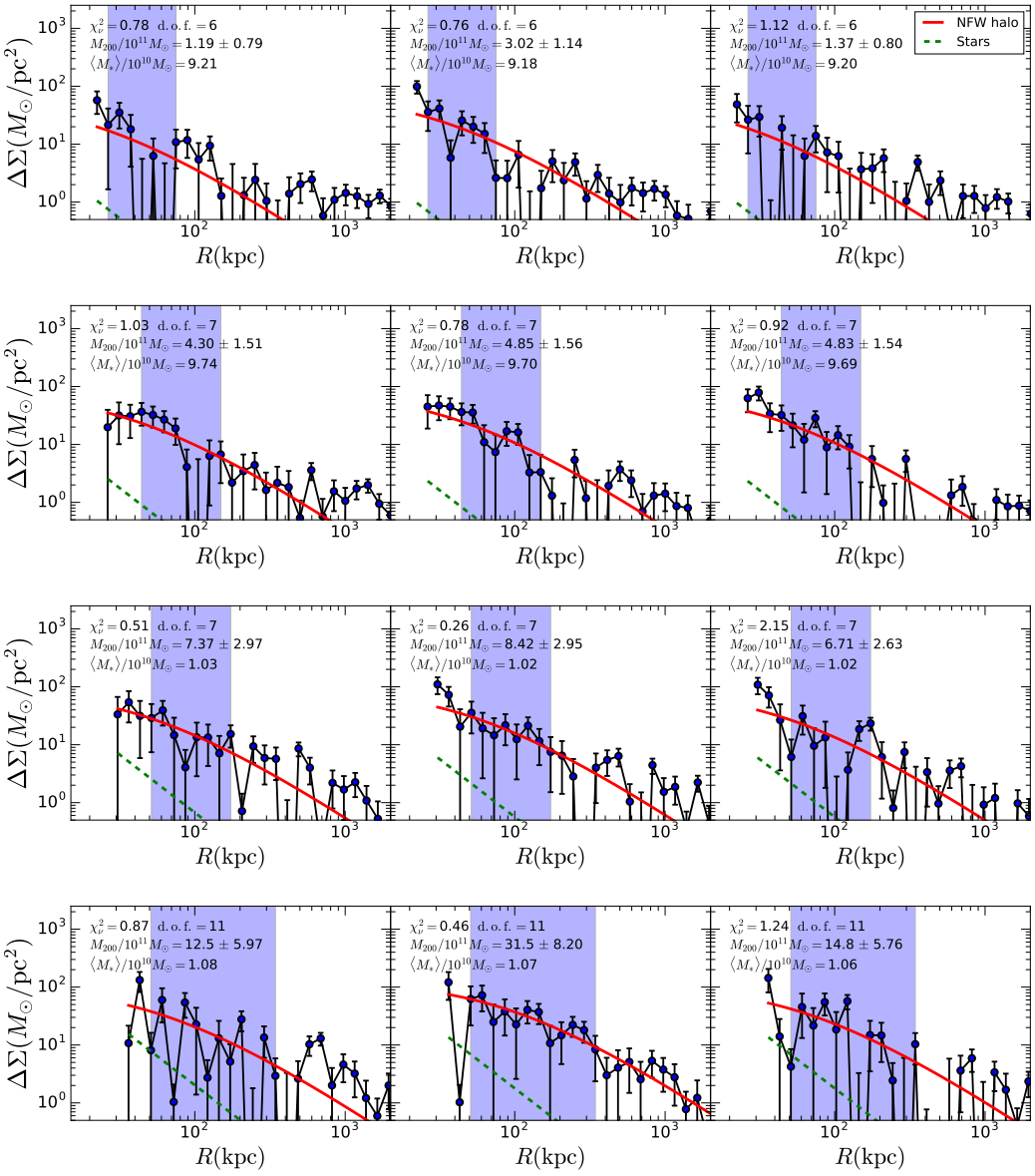

Figure 3.4: As in Figure 3.3 for blue lenses, $0.4 < z < 0.6$.

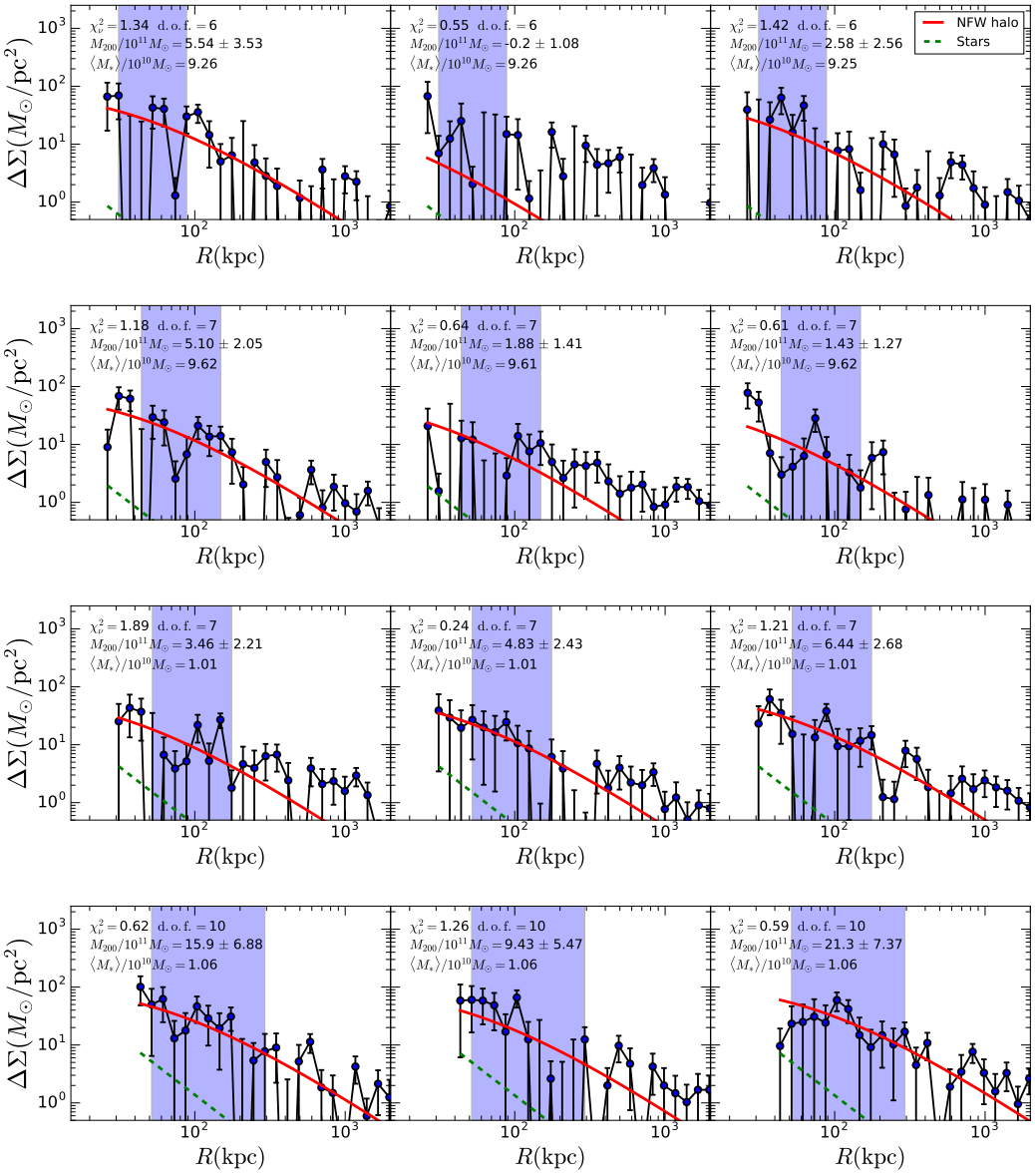

Figure 3.5: As in Figure 3.3 for blue lenses, $0.6 < z < 0.8$.

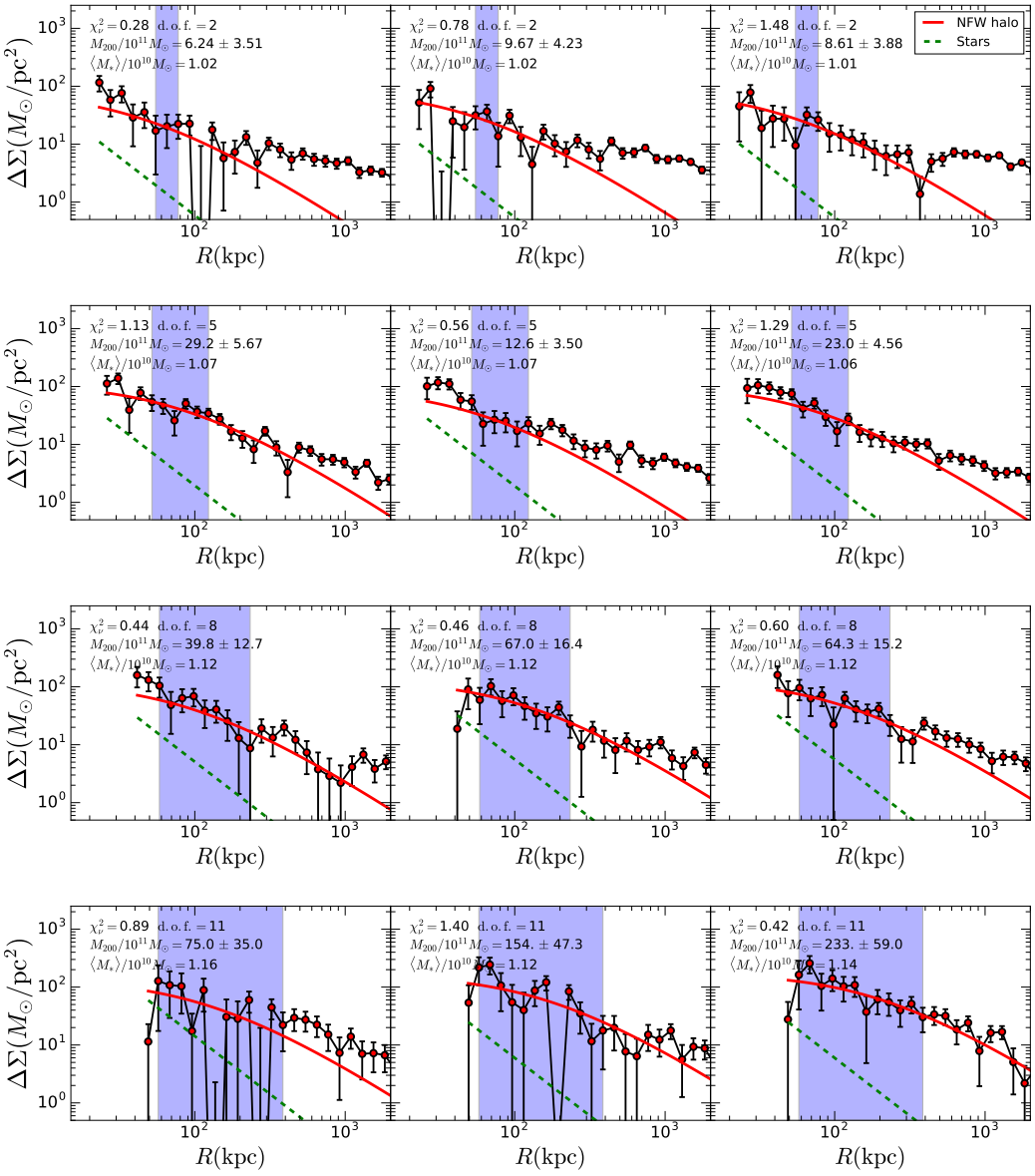

Figure 3.6: As in Figure 3.3 for red lenses, $0.2 < z < 0.4$.

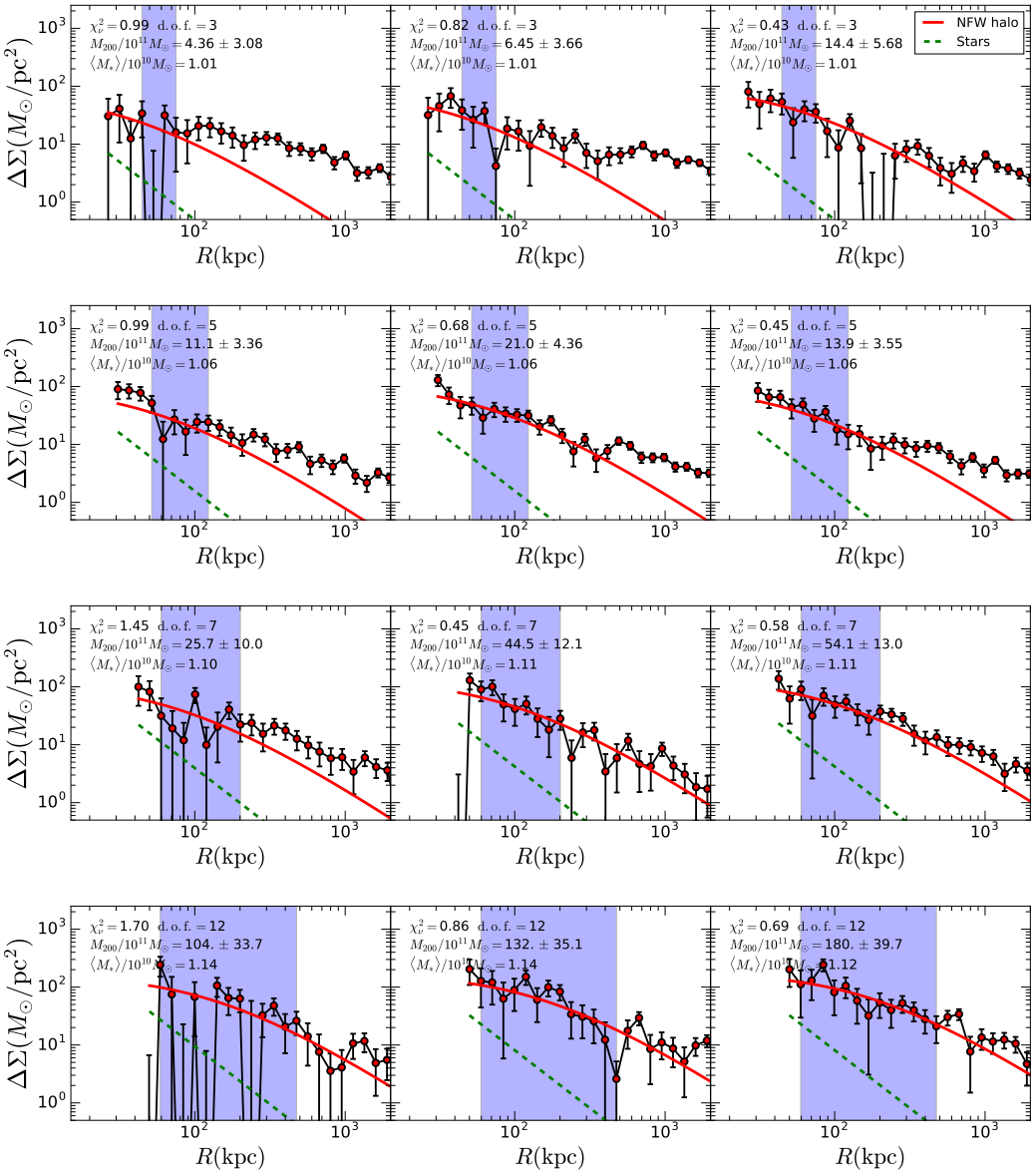

Figure 3.7: As in Figure 3.3 for red lenses, $0.4 < z < 0.6$.

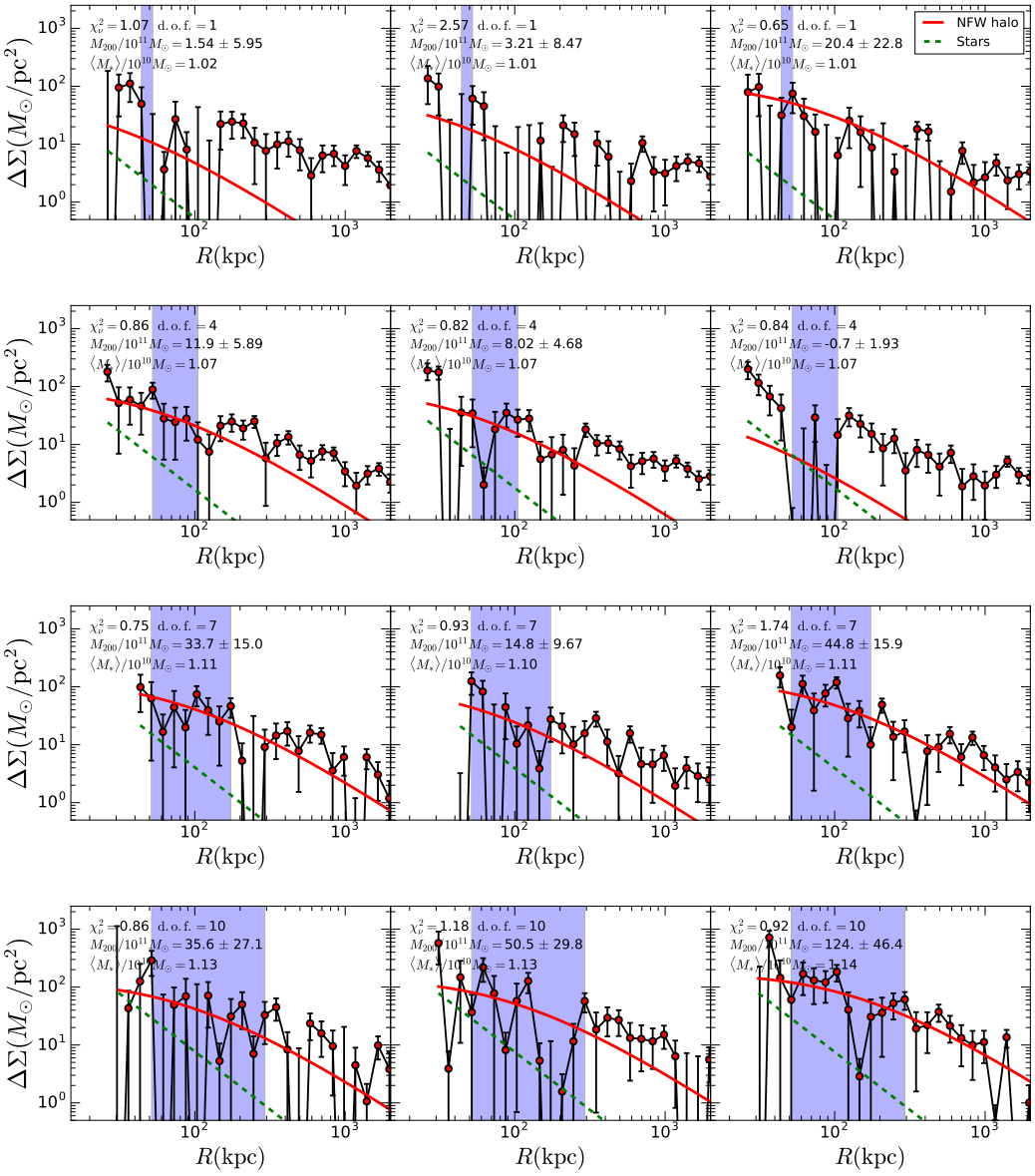

Figure 3.8: As in Figure 3.3 for red lenses, $0.6 < z < 0.8$.

the offset-group halo term requires information about the environments in which the lens galaxies reside. The approach used in Hudson et al. (2015) assumes a halo occupation distribution (HOD) using the method of Coupon et al. (2012) to recover a satellite fraction $f_{\rm sat}$, the expected fraction of galaxies of a given mass that reside in the halo of a larger group or galaxy. Using the same method here would be assuming that $r_{\rm eff}$ is not affected by environment. For example, if tidal stripping is responsible for $r_{\rm eff}$ differences, more stripped galaxies should reside closer to the centers of clusters. We elect not to fit the offset group term as doing so requires assumptions about the satellite fraction and radial distribution of satellites for subsamples of each size. For similar reasons, we do not truncate the one-halo term (Baltz et al. 2009), which arises for satellite galaxies due to stripping and their existence within a more massive halo.

We have restricted our fits to radii within which the offset-group term is sub-dominant to the one-halo term (see figures 2 and 3 in Hudson et al. 2015) and also wish to avoid extended light from the foreground galaxy affecting the quality of source shape measurements (Hudson et al. 1998;Velander et al. 2011). Boundaries are set using the fits from Hudson et al. 2015 as a guideline; the inner (stellar) boundary is set by the point where the NFW term is ten times greater than the stellar term, and the outer (group) boundary is set by where the NFW term is twice the offset-group term. Figures 3.3 through 3.8 show the three halo masses we fit for each size bin, highlighting in blue the range we fit over for each M_* and z_p bin. In some cases, the fitting regions may contain points with only negative $\Delta\Sigma$ values due to noisy source shapes. In these instances, we fit η using the remaining two size bins.

For each mass-colour-redshift bin we use equation 3.3 to fit the relationship between $\Delta M'_{\rm h}(M_*)$ and $\Delta r'_{\rm eff}(M_*)$ using our three size subsamples to find η. The intercept A should be 1 if the mass of our average size subsample matches our model, but this comes from the fits to central galaxies only. Our M_*-colour bins contain both centrals and satellites with possible differences in $f_{\rm sat}$ between size bins. $A \neq 1$ simply indicates that galaxies at the median size of a given stellar mass are not all centrals. Thus, to determine $\eta(M_*)$ we fit:

$$\Delta M'_{\rm h}(M_*) = \eta(M_*)\Delta r'_{\rm eff}(M_*) + \log_{10}(A) \tag{3.12}$$

Chapter 4

Results

Figures 4.1 and 4.2 show all η fits. We do not find any significant differences in η at different redshifts, so for each mass bin we combine our three z_p bins to create an average η weighted by the uncertainty of each z_p bin's η fit. The averaged values of η are shown in Figure 4.3 and table 4.1. Within 1σ, all of our stellar mass bins show a positive correlation between size and halo mass.

With the uncertainties in our η values, there does not appear to be a significant trend in η with stellar mass. If we simply average all mass and colour bins, we find $\langle\eta\rangle = 0.42 \pm 0.12$. The $\langle\eta\rangle$ of the blue galaxies is 0.28 ± 0.18, and $\langle\eta\rangle$ of the red galaxies is 0.53 ± 0.15. This indicates that, on average, there is a relationship between halo mass and size at fixed M_*. However, this correlation is weak, and can not account fully for the scatter in the SHMR (0.2). $\langle\Delta r'_{\rm eff}\rangle$ is approximately 0.15, giving

$$\langle\Delta M'_{\rm h}\rangle \approx \langle\eta\rangle\langle\Delta r'_{\rm eff}\rangle = 0.06 \tag{4.1}$$

just over 30% of the observed scatter.

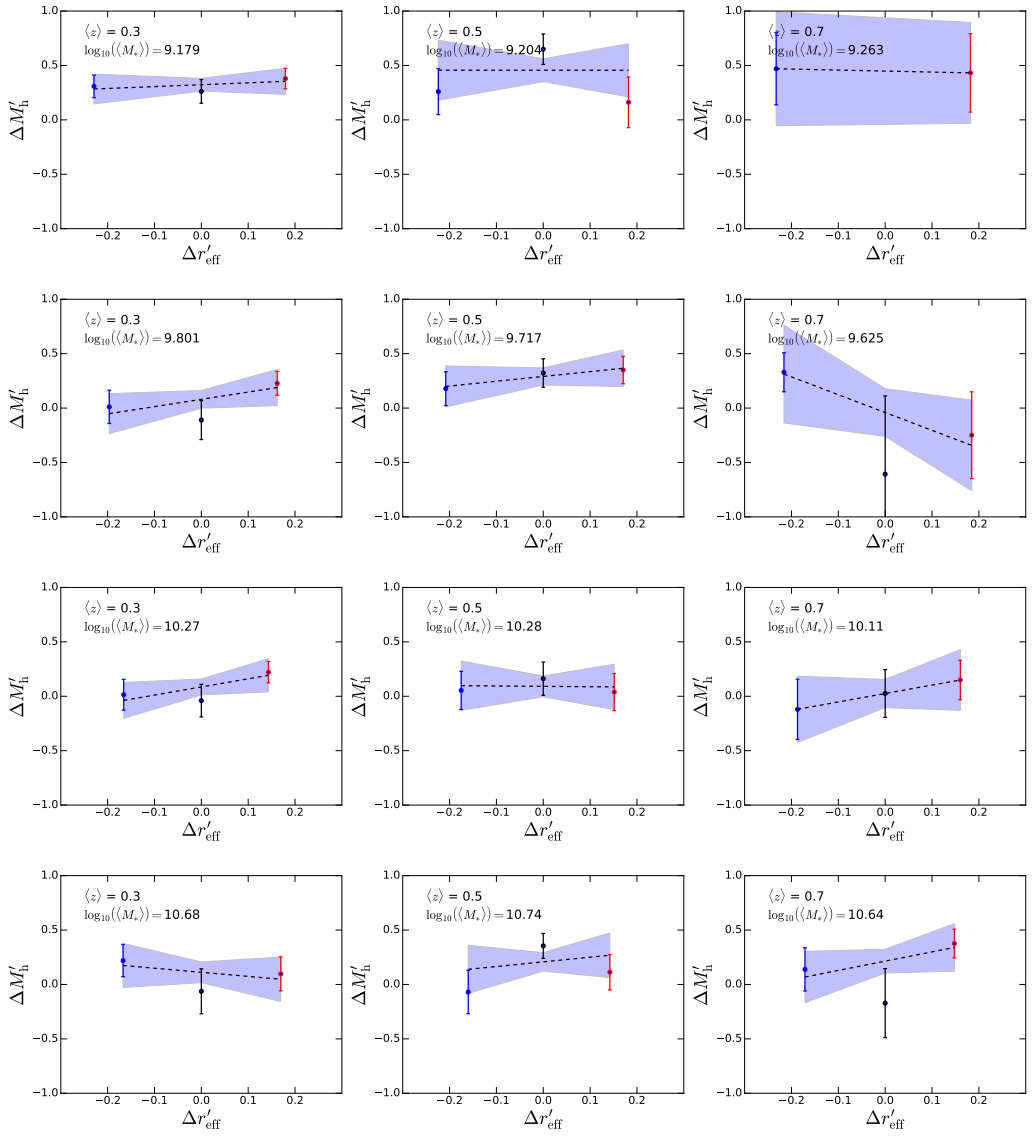

Figure 4.1: Plots of $\Delta r'_{\rm eff}$ versus $\Delta M'_{\rm h}$ used to fit η for our blue galaxy subsamples. The points are colour-coded to their coresponding size bin in Figure 3.2. Mass increases from top-to-bottom, redshift increases from left-to-right. The dashed black line indicates the best fit slope, and the shaded blue region indicates the 1σ region.

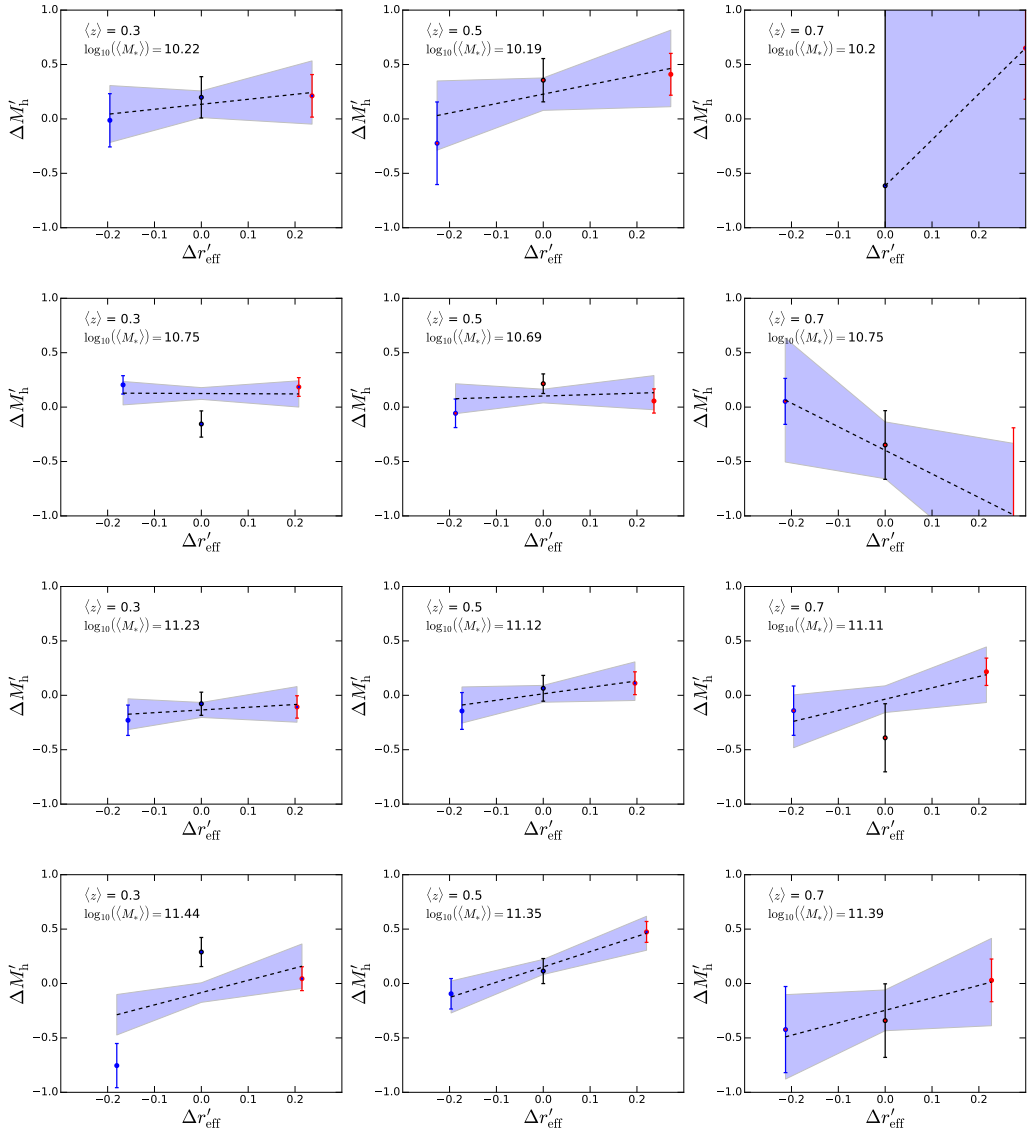

Figure 4.2: As in Figure 4.1 for our red galaxy subsample.

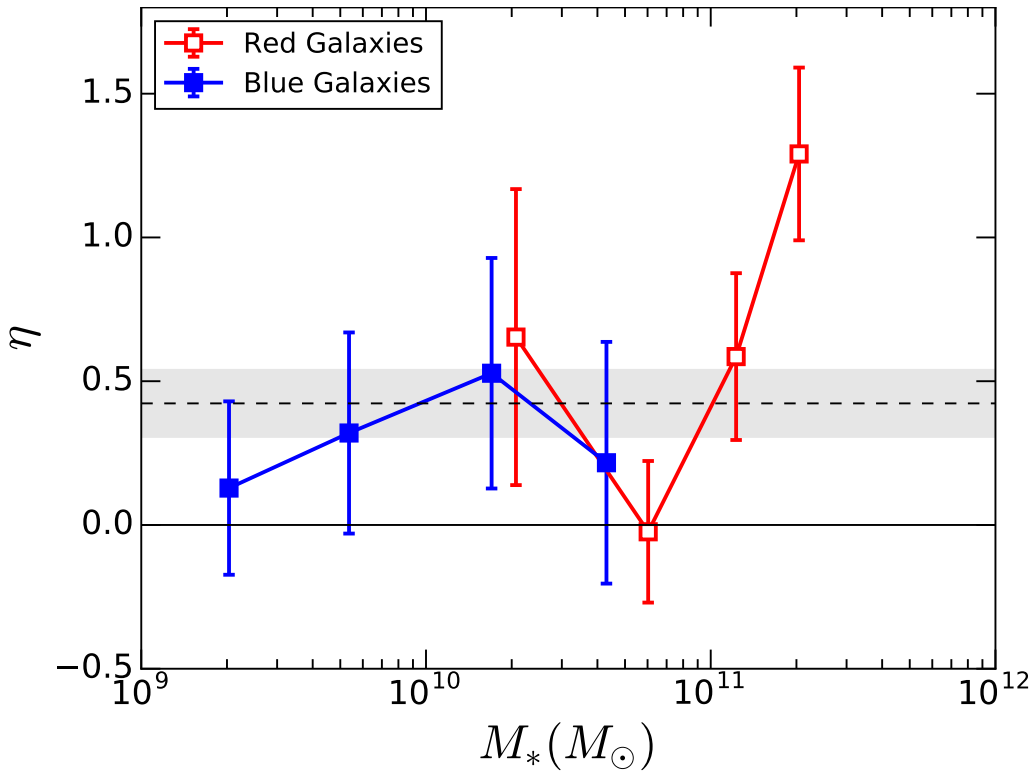

Figure 4.3: Average η for our red and blue galaxy samples. The fiducial average slope of all bins is plotted as the dashed black line, with the grey band representing the 1σ region. The points represent the weighted averages of the η values and average M_* of the galaxies each (z, M_*) bin.

Table 4.1: Halo mass-size fit results for our stacked galaxy bins. On the left of the vertical line are the details for each of our mass/redshift/colour bins, to the right of the line are the same bins, averaged over redshift.

Colour	z_p range	$\log_{10}(\langle M_* \rangle)$	η	$\log_{10}(\langle M_* \rangle_z)$	$\langle \eta \rangle$
Blue	$0.2 < z_p \leqslant 0.4$	9.231	0.17 ± 0.34		
Blue	$0.4 < z_p < 0.6$	9.279	0.00 ± 0.77	9.308	0.13 ± 0.30
Blue	$0.6 \leqslant z_p < 0.8$	9.398	-0.1 ± 1.2		
Blue	$0.2 < z_p \leqslant 0.4$	9.708	0.67 ± 0.52		
Blue	$0.4 < z_p < 0.6$	9.732	0.44 ± 0.53	9.730	0.32 ± 0.35
Blue	$0.6 \leqslant z_p < 0.8$	9.748	-1.6 ± 1.1		
Blue	$0.2 < z_p \leqslant 0.4$	10.241	0.75 ± 0.55		
Blue	$0.4 < z_p < 0.6$	10.220	-0.03 ± 0.75	10.230	0.53 ± 0.40
Blue	$0.6 \leqslant z_p < 0.8$	10.231	0.78 ± 0.93		
Blue	$0.2 < z_p \leqslant 0.4$	10.620	-0.38 ± 0.64		
Blue	$0.4 < z_p < 0.6$	10.620	0.43 ± 0.85	10.634	0.22 ± 0.42
Blue	$0.6 \leqslant z_p < 0.8$	10.660	0.85 ± 0.75		
Red	$0.2 < z_p \leqslant 0.4$	10.330	0.46 ± 0.71		
Red	$0.4 < z_p < 0.6$	10.301	0.87 ± 0.75	10.316	0.65 ± 0.52
Red	$0.2 < z_p \leqslant 0.4$	10.790	-0.02 ± 0.32		
Red	$0.4 < z_p < 0.6$	10.770	0.13 ± 0.40	10.780	-0.02 ± 0.25
Red	$0.6 \leqslant z_p < 0.8$	10.780	-2.2 ± 1.5		
Red	$0.2 < z_p \leqslant 0.4$	11.100	0.25 ± 0.46		
Red	$0.4 < z_p < 0.6$	11.077	0.59 ± 0.51	11.089	0.59 ± 0.29
Red	$0.6 \leqslant z_p < 0.8$	11.090	1.04 ± 0.61		
Red	$0.2 < z_p \leqslant 0.4$	11.290	1.13 ± 0.53		
Red	$0.4 < z_p < 0.6$	11.310	1.40 ± 0.39	11.310	1.29 ± 0.30
Red	$0.6 \leqslant z_p < 0.8$	11.330	1.15 ± 0.94		

Chapter 5

Comparison With Hydrodynamical Simulations

Due to the reliance of our weak lensing measurements upon stacking, we cannot examine η using individual lenses, and cannot measure the scatter around the trends that we fit. Our data also do not include environmental information, and one important factor we wish to investigate is whether η differs for central galaxies versus those in subhalos.

We investigate two hydrodynamical simulations, EAGLE (Schaye et al. 2015; Crain et al. 2015) and Illustris (Vogelsberger et al. 2014), which allows us to separately examine the size-halo mass trend for centrals and subhalos as well as determine what information is inaccessible due to the stacking and averaging required in order to perform our lensing analysis. Using the simulations, we wish to create a set of sample galaxy bins with broadly the same characteristics as our data. Each simulation has a snapshot at $z = 0.5$, the average redshift of our galaxy sample. We use the same method of splitting galaxies into subsamples by size as in our observations. We take the mean $M_{\rm h}$ of all galaxies in each size bin and compare that to $M_{\rm h,exp}(\langle M_* \rangle)$.

Galaxies are divided by colour in a manner similar to the data; each simulation includes stellar luminosities in the SDSS *ugriz* filters. We look for bimodality in the colour distributions, as we do with our data, in order to separate the simulated galaxies into red and blue samples. It is worth noting that the luminosities in our catalogue are corrected for dust extinction, while

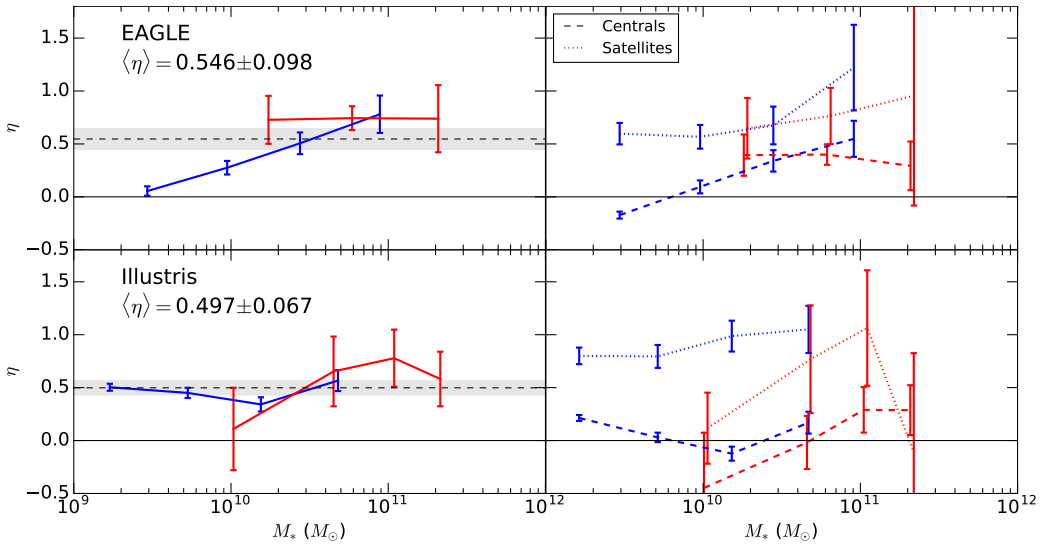

Figure 5.1: Halo mass-size dependence for the simulations examined. Top row: EAGLE, bottom row: Illustris. Left: Mass bins without splitting by environment, includes fiducial average. Right: The same mass bins split into satellite galaxies and central galaxies, dashed lines represent centrals, dotted lines represent satellites. The red central masses have been shifted 5% lower for clarity. The average η has not been weighted by the individual errors due to the comparatively large difference in σ_η between M_* bins relative to the data.

the simulated galaxies' magnitudes explicitly exclude dust. Slight differences in the mass-to-light ratio lead to differences in the average stellar mass of galaxies in each bin across the simulations and data, but they broadly cover the same ranges.

Rather than use a half-light radius from simulated observations, we use the half-stellar mass radius for our sizes. EAGLE's catalogues include both the 3D and projected half-mass radius. We use the projected radii for a more direct comparison to our observations. Illustris includes only the 3D half-mass radius. Investgating the difference using the EAGLE galaxies shows that the 3D radii are on average 30% larger than the projected radius, with no change as a function of M_*. There is also no significant difference in size between subhaloes and centrals. Since our η relies on a differential measurement of size, we consider Illustris' $r_{\mathrm{eff,M_*,3D}}$ acceptable for our purposes under the assumption that the same relationship holds.

There are some considerations to take into account with these simulations. Both have a volume on the order of 100 Mpc, which limits the number of galaxies in our high mass bins. For this reason, the error bars on the fitted η of the highest M_* bins should not be trusted implicitly, as the precision of some of the statistics is overestimated due to the low number of galaxies. Illustris is also known to be in disagreement with several observed properties of galaxy populations: The luminosity-size relationship is too shallow at high masses, and flattens at low masses; there is also a lack of low-mass bulge galaxies (Bottrell et al. 2017). The fits to the simulated galaxies are summarized in Figure 5.1; values and fits for each stellar mass bin are tabulated and shown in appendix B.

5.1 Simulation Results

Figure 5.2 shows our fitted η values from the CFHTLenS overlaid on the range of slopes covered by the two hydrodynamical simulations we examined. Our data lie within 1σ of the range spanned by the simulations. We can draw several clear conclusions from the simulations:

1. Satellite galaxies universally show a stronger $\Delta M'_{\mathrm{h}}$-$\Delta r'_{\mathrm{eff}}$ relationship than centrals. η_{sat} lies in the range of 0.5-1.0 while η_{cent} is generally

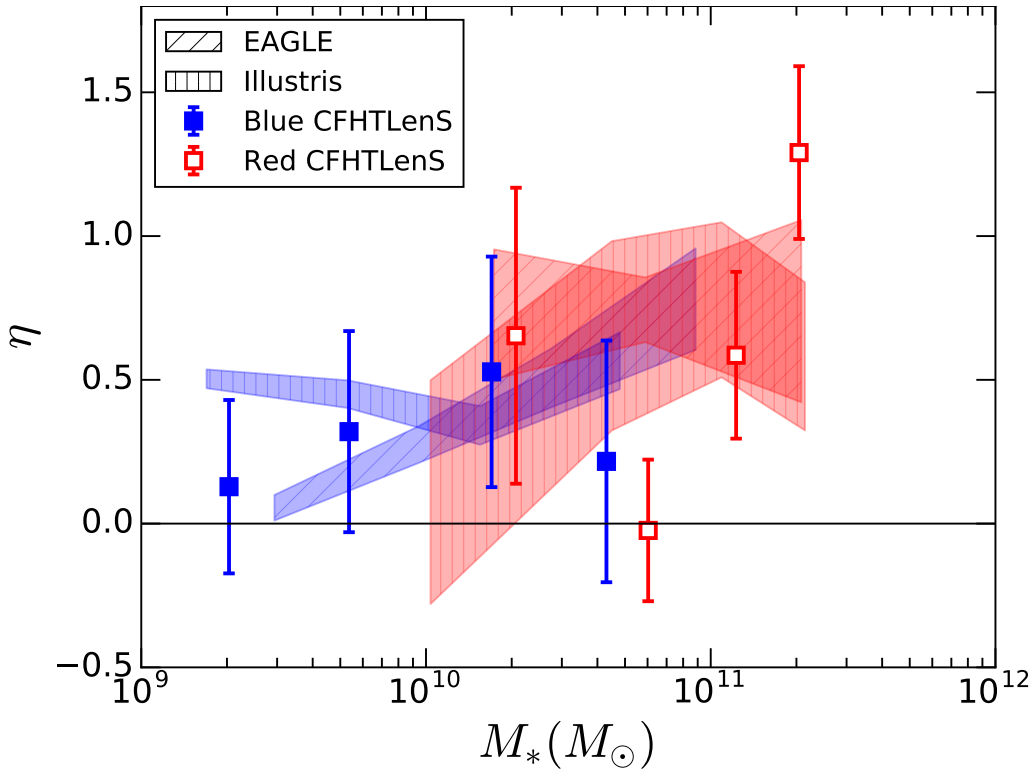

Figure 5.2: Halo mass-size dependence for EAGLE's and Illustris' red and blue galaxy samples without spitting by environment. Our data is overlaid on the range covered by the simulation slopes + errors (shaded regions). Filled symbols are blue galaxies and open symbols are red galaxies. The simulations and our data agree within 1σ.

between 0-0.5.

2. The simulations show that the scatter in the $\Delta M'_{\rm h}$-$\Delta r'_{\rm eff}$ relationship is much tighter for central galaxies than for satellites. A likely reason for this is the large variety of processes capable of influencing each parameter in the cluster environment when compared to galaxies in the field or at the cluster center, such as tidal stripping, ram pressure stripping, and harassment.

3. In most M_* bins, central/field galaxies dominate the population. However, bins with higher satellite fractions do not have significantly higher η. This is likely due to the more tightly correlated central halo relationship dominating the fit.

4. In general, the η of the simulations are broadly consistent with each other.

5. Where the simulations do differ is in low mass red and blue galaxies. At low mass, Illustris blue galaxies show a greater η than EAGLE, while Illustris red galaxies show a lower η than EAGLE.

Chapter 6

Discussion

We have found that η is generally positive, and this result is also seen in the EAGLE and Illustris simulations. In this section we consider several physical effects that may be responsible for this. To model how halo mass and size may be related, we examine how specific processes could change the position of a given galaxy on a plot of $\Delta M'_{\rm h}$ vs $\Delta r'_{\rm eff}$. We consider both effects due to initial conditions and in situ evolution, and envrionmental effects, due to interactions with other galaxies or due to the cluster environment. From the simulations we expect that satellite and central galaxies will have different η.

6.1 Concentration

Simulations show that halos are denser at earlier times (Bullock et al. 2001; Hearin & Watson 2013). Broadly, the highest amplitude density fluctuations collapse first, when the characteristic scale factor a is smaller than later times. To account for this evolution, our NFW halo model has a concentration c_{200} which is not a free parameter, but is determined by the lens' $z_{\rm p}$ and M_h (see Section 3.5.2). There is, however, a degeneracy between M_h and c_{200}. For example, Gillis et al. (2013) illustrates that a halo of $\log_{10}(M_{\rm h}) = 11.6$ with $c_{200} = 8$ can generate the same lensing signal as a halo of $\log_{10}(M_{\rm h}) = 11.7$ with $c_{200} = 4$. To break the degeneracy between M_h and c_{200}, we require more information about the shape of the NFW profile. Our models of the

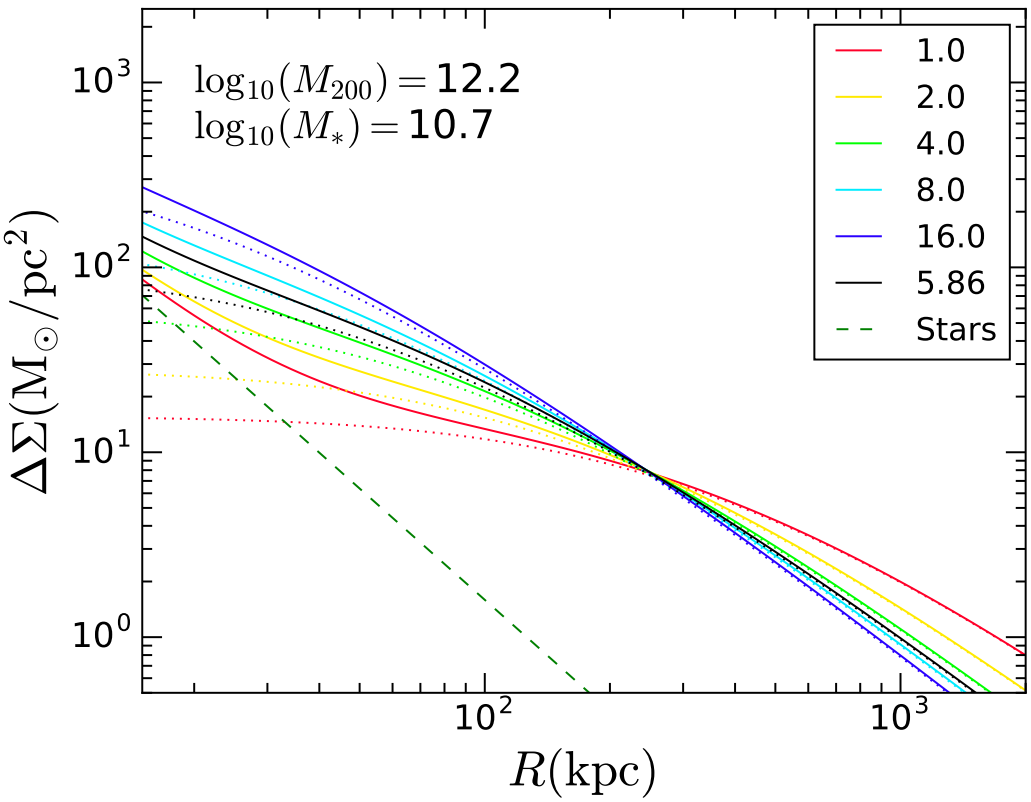

Figure 6.1: Excess surface density plot illustrating how c_{200} can appear to shift the one-halo term's normalization at small radii. M_h and M_* remain fixed. The colours indicate different values of c_{200}. The radius at which all profiles meet is r_{eq}. The dotted lines are the NFW halos alone, and the solid lines are the combined NFW+ stars. The black lines indicate the profile for the expected halo concentration of a galaxy of this mass at $z = 0.5$. Note that $c_{200} \lesssim 4$ are not realistic and are included for illustration only.

outer halo are limited by our ability to fit meaningful offset-group halo terms and the necessity of stacking.

If we fix M_h for each of our lens bins using the SHMR fits of Hudson et al. (2015) we can shift the NFW component's normalization and slightly alter its shape by changing c_{200}, illustrated in Figure 6.1. At a certain radius $r_{\rm eq}$ all concentrations will have the same $\Delta\Sigma$ value ($\sim 100-300$kpc over our M_* range). More (less) concentrated halos have more (less) mass contained within $r_{\rm eq}$, which is capable of mimicking a more (less) massive halo if the fit depends primarily upon radial bins within $r_{\rm eq}$. Were we to create an $\eta_{\rm c}$ holding $M_{\rm h}$ fixed, using $\Delta c'_{200}$ instead of $\Delta r'_{\rm eff}$, it would likely look similar to η unless we were able to constrain the concentration with measurements at large radii.

The link between concentration and mass accretion rate in N-body simulations is shown in e.g. Wechsler et al. (2002); for halos of a fixed total mass at the present time, older halos have higher concentrations. This can, for example explain scatter in M_h for a fixed M_* in EAGLE (Matthee et al. 2017) but must be tied to galaxy size to explain η. We know that the density of star forming gas is tied to the star formation rate through the Kennicutt-Schmidt relationship (Schmidt 1959; Kennicutt 1998). Since the dark matter halo is the majority of the galaxy's mass, to first order we expect that it should establish the gravitational potential that star-forming gas responds to. In this way, a more concentrated halo should contain more concentrated stars, leading to a smaller $r_{\rm eff}$ while a less concentrated halo should host a larger galaxy.

6.2 Mergers

The role of galaxy mergers in the halo mass-size relationship should be treated with consideration of several factors: whether the galaxy lives in a high density or low density environment, is a disk or elliptical-type, and mass ratios of past mergers. In general we expect mergers will increase both the size and mass of the resultant galaxy, but the amount can vary based on the above factors. To first order, galaxies that have gone through more mergers should be larger and have more massive halos and stellar components. In order to account for the observed halo mass-size relationship, we must consider how

to create a range of halo masses and sizes while keeping stellar mass relatively fixed.

The bin with the largest η is our highest M_* red bin which contains mostly LRGs. Evidence suggests that minor mergers (along with in situ star formation) account for the majority of the present day mass growth of central cluster/group galaxies with major mergers only becoming important at the present day (Groenewald et al. 2017). Naab et al. (2009) describes the rate of size growth or elliptical galaxies due to minor mergers. As mergers occur, stellar mass is distributed outward leading to size growth. The equation describing the growth in size after accretion is:

$$\frac{\langle r_f^2 \rangle}{\langle r_i^2 \rangle} = \frac{(1+\lambda)^2}{(1+\lambda\epsilon)} \tag{6.1}$$

where λ is the ratio between the initial stellar mass and the accreted stellar mass and ϵ is the ratio of mean squared speeds of the accreted material to the initial material (this is ˜1 for major mergers, and ˜0 for minor mergers). As a baseline, we look at a galaxy doubling its stellar mass through mergers; if all mergers are minor mergers this leads to a factor of four increase in size and if this occurs through major mergers the galaxy doubles in size. This first order approximation assumes that all stars and dark matter are accreted and that the galaxy has time to virialize between each merger.

The size increase described above is for centrals. Thus as an example we consider a galaxy doubling in mass to the middle of our largest mass bin, mainly containing LRGs, given the stellar mass range. We need to know the growth of both $r_{\rm eff}$ and $M_{\rm h}$ at a fixed M_*:

$$\Delta \log_{10}(r_{\rm eff})\,|_{M_*} = \Delta \log_{10}(r_{\rm eff}) - \alpha \Delta \log_{10}(M_*) \tag{6.2}$$

α for red galaxies is taken from our $r_{\rm eff} - M_*$ fits (see appendix A). Following equation 6.1 for minor mergers:

$$\Delta \log_{10}(r_{\rm eff})\,|_{M_*} = \log_{10}\left(\frac{4 r_{\rm eff,i}}{r_{\rm eff,i}}\right) - 0.29 \log_{10}\left(\frac{2 M_{*,\rm i}}{M_{*,\rm i}}\right) \tag{6.3}$$

and for halo mass:

$$\Delta \log_{10}(M_{\rm h})\,|_{M_*} = \Delta \log_{10}(M_{\rm h}) - s_{\rm h}(M_*)\,\Delta \log_{10}(M_*) \tag{6.4}$$

Where $s_{\rm h}(M_*)$ is the slope of the $M_* - M_{\rm h}$ relationship at fixed M_*. This comes from the model used to determine our expected $M_{\rm h}$ discussed in section 3.4. The halo mass growth depends on the assumptions made for the SHMR of accreted galaxies. A simple approximation is to assume that on average, we can use the universal fraction of baryons in stars:

$$\gamma = \frac{\Omega_*}{\Omega_m} = \frac{0.0018}{0.30} \tag{6.5}$$

We use the value of Ω_* as determined by GAMA (Moffett et al. 2016). Thus the growth of $M_{\rm h}$ is

$$M_{{\rm h},f} = \left(\frac{1}{\gamma} + \frac{1}{f(M_*)}\right) M_* \tag{6.6}$$

Where $f(M_{*,i})$ is the SHMR at the initial M_*. The change in $M_{\rm h}$ is

$$\Delta \log_{10}(M_{\rm h}) = \log_{10}\left(1 + \frac{f}{\gamma}\right) \tag{6.7}$$

and equation 6.4 becomes

$$\Delta \log_{10}(M_{\rm h})\,|_{M_*} = \log_{10}\left(1 + \frac{f}{\gamma}\right) - s_{\rm h}(M_*) \log_{10}\left(\frac{2M_{*,i}}{M_{*,i}}\right) \tag{6.8}$$

For a galaxy in our highest M_* bin, this leads to $\eta \approx 1$, within 1σ of the η we observe for LRGs.

The above is a simple case where all accreted galaxies are close to the universal baryon ratio. In a more realistic model, the mass distribution of mergers experienced by the galaxy are likely to follow a Press & Schechter (1974) mass function truncated at the original galaxy's mass (e.g. Gao et al. 2004; McBride et al. 2009). Since our simplified model assumes all mergers are minor, a more realistic model will have more mergers at a mass ratio closer to 1, thus we expect the true η should be lower.

Another simplification we made is to assume that mergers happen instantaneously. The stellar mass will take time to merge, so $r_{\rm eff}$ will not immediately quadruple while they remain separated. The halos of the infalling satellites will be stripped first and join the halo of the central galaxy. What this leads to is a greater than expected $M_{\rm h}$ while $r_{\rm eff}$ remains at closer to the original value. Due to this, we can consider the η in our toy model to be a lower limit.

6.3 Stripping

Stripping is predicted to play a large role in the ηs we observe for satellites. The high density of galaxies in clusters provide ample opportunities for tidal stripping, while at the same time galaxies experience ram-pressure stripping due to the intracluster medium. These two stripping processes are likely to occur simultaneously, making analytical modeling difficult. We examine them in isolation, taking this into consideration for any conclusions we draw.

Tidal stripping is the removal of material due to close interactions with other galaxies in the cluster, with with the least bound matter stripped off first. Since dark matter halos appear to be much greater in extent than the stellar portions of galaxies, for the first few Gyr within the cluster, tidal interactions preferentially strip the dark matter halo (Chang et al. 2013; Smith et al. 2016) and some gas (Balogh et al. 2000) while leaving the stars relatively intact. Tidal stripping effectively truncates the dark matter halo and reduces its mass. Eventually, continued tidal stripping removes significant amounts of both stars and dark matter, and galaxies will continue to evolve to lower halo masses, moving to smaller sizes as well. In the absence of mergers and accretion this could lead to galaxies moving to different stellar mass bins.

The most straightforward way that tidal stripping alone would affect galaxies in our $M_{\rm h}$-$r_{\rm eff}$ plots would be to, over time, move a galaxy to lower halo masses. For a satellite of a given M_*, the larger $r_{\rm eff}$ is, the less its halo can be stripped before removing stellar mass, so smaller satellites are able to have more of their halo stripped, reducing their halo mass in comparison to their larger counterparts. This effect would correspond to a positive η.

A galaxy moving through the intracluster medium will experience a pressure that depends on the density of the medium and its velocity, so-called ram-pressure, that will preferentially strip star forming gas, i.e. ram-pressure stripping (Gunn & Gott 1972). The ram pressure first strips the lower density gas in the outer regions of the galaxy, depositing it into a wake. This leads to reduced star formation within the galaxy, and, over time, a reduced size (Kapferer et al. 2009). Dark matter is unaffected by ram pressure, however two stripping mechanisms could work in tandem; reducing $M_{\rm h}$ through tides, and $r_{\rm eff}$ through ram pressure to create a positive η.

6.4 Angular momentum

It is theorized that galactic disks exist due to rotational support created by torques during formation and accretion of smaller galaxies. Whether considering individual clouds of material in the early universe or accreted material, baryons and dark matter both have angular momentum but only the baryons are capable of dissipating it. The model of Fall & Efstathiou (1980) showed that a disk's final scale radius is related to the primordial spin (Peebles 1969) of its baryon/dark matter cloud. For two galaxies of equal $M_{\rm h}$ and primordial star-forming gas mass, the halo with more angular momentum will form a larger galaxy with lower gas surface density and, by the Kennicutt-Schmidt relationship, less mass in stars. A more massive halo with proportionally more gas could conceivably form a larger galaxy at a fixed M_* today, thus creating a positive η.

The above analysis concludes that the η of disk galaxies should be most affected by angular momentum, however there is evidence to suggest that, instead, isolated (or low density environment) disk galaxies see no correlation between $M_{\rm h}$ and $r_{\rm eff}$. Lelli et al. (2016) perform a similar analysis to our own, using the baryonic Tully-Fisher relationship. This is consistent with the central blue galaxies in Illustris (though not EAGLE) and likely indicates that, at least in blue galaxies, η is not strongly affected by a halo's initial angular momentum.

Chapter 7

Conclusion

In this section we summarize the results of our analysis of the data and the comparison with the simulations (7.1). We also discuss possibilities for expanding and improving upon the results obtained this work (7.2).

7.1 Summary of results

We have obtained sizes for more than 2×10^6 CFHT Legacy Survey lens galaxies, and used 5.6×10^6 source galaxy shape measurements from CFHTLenS to determine the relationship between a galaxy's size and its dark matter halo mass at a fixed M_* for galaxies between $10^9 M_\odot$ and $3 \times 10^{11}\odot$. This is the first work to provide observational evidence for a correlation of this nature. The relationship takes the form of $M_{\rm h} \propto r_{\rm eff}^{\eta}$. The conclusions we draw are:

1. The weighted average η across all M_* bins is 0.42 ± 0.16 indicating a positive correlation between size and halo mass.
2. We do not detect a strong evolutionary trend across our three z_p bins centered at 0.2, 0.4, and 0.6.
3. η is largest in our high M_* bin containing mostly LRGs, but the uncertainties on our other η measurements do not permit us to make a strong statement for trends with stellar mass.

4. Our η are consistent with the two hydrodynamical simulations we compared with for all but the most massive galaxies. The limited size of the simulation boxes (100Mpc) allows only very few high mass galaxies to form, limiting the accuracy of any fits to their $\Delta M'_{\rm h}$-$\Delta r'_{\rm eff}$ relationship.

5. The simulations indicate that the η for satellites is significantly higher than for central galaxies. They also show that the scatter in the $\Delta M'_{\rm h}$-$\Delta r'_{\rm eff}$ relationship is much tighter for centrals than for satellites. This indicates that there are likely more processes driving η for satellite galaxies, such as frequent tidal interactions with other galaxies, and interaction with the intracluster medium stripping the stars and dark matter from cluster members.

6. We show that mergers can partially explain the η for central elliptical galaxies, and provide a lower limit for η.

The detection of a relationship between size and halo mass may warrant revisiting studies of scaling relations as they relate to the halo. For instance, Courteau & Rix (1999) assume that the disk is uncorrelated with the initial halo's structure and Dutton et al. (2013) adopt a fixed disk mass to halo mass ratio, and both find a weak negative correlation in residuals between velocity-mass and size-mass relations. Combining our own relation, $M_{\rm h} \propto r_{\rm eff}^{\eta}$ with the virial theorem $V_{200} \propto M_{200}^{1/3}$ under the assumption that $V_{\rm disk}$ is a fixed fraction of V_{200} indicates that

$$\frac{\partial \log_{10} V_{\rm disk}}{\partial \log_{10} r_{\rm eff}} = \frac{\eta}{3} \tag{7.1}$$

7.2 Further Directions

Future approaches to investigating the halo mass-size relationship will require further observations. Two obvious improvements are an expanded lens and source catalogue which will allow a more fine-grained investigation of η, at more sizes and masses, and information about whether each lens is a central galaxy or a satellite.

7.2.1 Expanded data set

In order to avoid overwhelming shape noise we were restricted to dividing our data into three size bins and using four mass bins. In comparison to Hudson et al. (2015) the uncertainty of our halo masses are increased by a factor of $\sim \sqrt{3}$ due to this subsampling. Several upcoming surveys present opportunities for improved analysis. Improvements primarly come from an expanded area and volume, increasing the number of lenses and sources.

- The Kilo Degree Survey (KiDS) covers nearly 10 times the area of CFHTLS Wide, slightly shallower, and in a similar analysis to this work could reduce lensing mass uncertainties by a factor of three.
- CFIS is the next-generation of the CFHTLenS survey covering 30 times the area; though not as deep, this could provide up to a factor of five improvement in precision.
- Several space-based lensing surveys are also upcoming, which have the advantage of increased volume, providing more sources per lens. WFIRST is a deep survey which can provide extremely accurate shape measurements for sources at high redshifts, which decreases the shape measurement error instead of the shape noise. Another, Euclid, is designed to image nearly 100 times the area of CFHTS Wide to a greater depth, with the possibility of improving upon these results by a factor of 10.

7.2.2 Environmental information

The ability to investigate η for satellite and central galaxies separately will be instrumental in further work on this topic. As discussed previously, we expect different processes to act upon each category, which may lead to a different η. We also require this information in order to improve our halo modeling. Satellites have truncated one-halo terms and a large offset-group term in the lesning signal, as opposed to the signal of central galaxies which only contain contributions from their own, untruncated halo. It is also incorrect to assume that each size bin will have the same satellite fraction, further complicating current attempts to do this based on the statistics of simulations.

The CFHTLenS catalogues contain some infomation that would allow

us to investigate environment as illustrated in Gillis & Hudson (2011) and applied in Gillis et al. (2013)). To assist with this we would benefit from spectroscopic redshift measurements which are more robust, but expensive and time consuming to obtain. Surveys of this nature are upcoming, and some large surveys, such as CFIS, are designed to overlap with existing spectral surveys, and will allow a catalogue of lenses by environment to be created where coverage with lensing surveys permits. The most immediate improvements will be to high stellar mass subsamples containing, at most, several thousand lenses, rather than low mass galaxies containing tens or hundreds of thousands of lenses.

Bibliography

Balogh M. L., Navarro J. F., Morris S. L., 2000, ApJ, 540, 113

Baltz E. A., Marshall P., Oguri M., 2009, J. Cosmology Astropart. Phys., 1, 015

Bartelmann M., 1996, A&A, 313, 697

Behroozi P. S., Conroy C., Wechsler R. H., 2010, ApJ, 717, 379

Behroozi P. S., Wechsler R. H., Conroy C., 2013, ApJ, 770, 57

Bernardi M., Hyde J. B., Sheth R. K., Miller C. J., Nichol R. C., 2007, AJ, 133, 1741

Blumenthal G. R., Faber S. M., Primack J. R., Rees M. J., 1984, Nature, 311, 517

Bond J. R., Cole S., Efstathiou G., Kaiser N., 1991, ApJ, 379, 440

Bottrell C., Torrey P., Simard L., Ellison S. L., 2017, preprint, (`arXiv:1701.08206`)

Brainerd T. G., Blandford R. D., Smail I., 1996, ApJ, 466, 623

Bruzual G., Charlot S., 2003, MNRAS, 344, 1000

Bullock J. S., Kolatt T. S., Sigad Y., Somerville R. S., Kravtsov A. V., Klypin A. A., Primack J. R., Dekel A., 2001, MNRAS, 321, 559

Chabrier G., 2003, PASP, 115, 763

Chang J., Macciò A. V., Kang X., 2013, MNRAS, 431, 3533

Ciotti L., 1991, A&A, 249, 99

Conroy C., Wechsler R. H., Kravtsov A. V., 2006, ApJ, 647, 201

Coupon J., et al., 2012, A&A, 542, A5

Courteau S., Rix H.-W., 1999, ApJ, 513, 561

Courteau S., et al., 2014, Reviews of Modern Physics, 86, 47

Covington M., Dekel A., Cox T. J., Jonsson P., Primack J. R., 2008, MNRAS, 384, 94

Crain R. A., et al., 2015, MNRAS, 450, 1937

Dalla Vecchia C., Schaye J., 2012, MNRAS, 426, 140

Davis M., et al., 2007, ApJ, 660, L1

Dekel A., Cox T. J., 2006, MNRAS, 370, 1445

Dekel A., Sari R., Ceverino D., 2009, ApJ, 703, 785

Djorgovski S., Davis M., 1987, ApJ, 313, 59

Dressler A., Lynden-Bell D., Burstein D., Davies R. L., Faber S. M., Terlevich R., Wegner G., 1987, ApJ, 313, 42

Dutton A. A., Courteau S., de Jong R., Carignan C., 2005, ApJ, 619, 218

Dutton A. A., et al., 2011, MNRAS, 410, 1660

Dutton A. A., Macciò A. V., Mendel J. T., Simard L., 2013, MNRAS, 432, 2496

Erben T., et al., 2013, MNRAS, 433, 2545

Faber S. M., Gallagher J. S., 1979, ARA&A, 17, 135

Fahlman G., Kaiser N., Squires G., Woods D., 1994, ApJ, 437, 56

Fall S. M., Efstathiou G., 1980, MNRAS, 193, 189

Freeman K. C., 1970a, ApJ, 160, 811

Freeman K. C., 1970b, ApJ, 161, 802

Gao L., White S. D. M., Jenkins A., Stoehr F., Springel V., 2004, MNRAS, 355, 819

Gerhard O., Kronawitter A., Saglia R. P., Bender R., 2001, AJ, 121, 1936

Gerritsen J. P. E., 1997, PhD thesis, , Groningen University, the Netherlands, (1997)

Gillis B. R., Hudson M. J., 2011, MNRAS, 410, 13

Gillis B. R., et al., 2013, MNRAS, 431, 1439

Graham A. W., Driver S. P., 2005, PASA, 22, 118

Griffith R. L., et al., 2012, ApJS, 200, 9

Groenewald D. N., Skelton R. E., Gilbank D. G., Ilani Loubser S., 2017, preprint, (`arXiv:1701.09012`)

Gunn J. E., Gott III J. R., 1972, ApJ, 176, 1

Häussler B., et al., 2007, ApJS, 172, 615

Hearin A. P., Watson D. F., 2013, MNRAS, 435, 1313

Heymans C., et al., 2012, MNRAS, 427, 146

Heymans C., et al., 2013, MNRAS, 432, 2433

Hildebrandt H., et al., 2012, MNRAS, 421, 2355

Huang K.-H., et al., 2017, ApJ, 838, 6

Hudson M. J., Gwyn S. D. J., Dahle H., Kaiser N., 1998, ApJ, 503, 531

Hudson M. J., et al., 2015, MNRAS, 447, 298

Ilbert O., et al., 2006, A&A, 457, 841

Kapferer W., Sluka C., Schindler S., Ferrari C., Ziegler B., 2009, A&A, 499, 87

Kennicutt Jr. R. C., 1998, ApJ, 498, 541

Kravtsov A. V., 2013, ApJ, 764, L31

Kravtsov A. V., Berlind A. A., Wechsler R. H., Klypin A. A., Gottlöber S., Allgood B., Primack J. R., 2004, ApJ, 609, 35

Lacey C., Cole S., 1993, MNRAS, 262, 627

Lelli F., McGaugh S. S., Schombert J. M., 2016, ApJ, 816, L14

Mandelbaum R., Seljak U., Kauffmann G., Hirata C. M., Brinkmann J., 2006, MNRAS, 368, 715

Marinoni C., Hudson M. J., 2002, ApJ, 569, 101

Matthee J., Schaye J., Crain R. A., Schaller M., Bower R., Theuns T., 2017, MNRAS, 465, 2381

McBride J., Fakhouri O., Ma C.-P., 2009, MNRAS, 398, 1858

McGaugh S. S., Schombert J. M., Bothun G. D., de Blok W. J. G., 1999, in American Astronomical Society Meeting Abstracts. p. 1559

McGaugh S. S., Schombert J. M., Bothun G. D., de Blok W. J. G., 2000, ApJ, 533, L99

Miller L., et al., 2013, MNRAS, 429, 2858

Miralda-Escude J., 1991, ApJ, 370, 1

Mo H. J., Mao S., White S. D. M., 1998, MNRAS, 295, 319

Mo H., van den Bosch F. C., White S., 2010, Galaxy Formation and Evolution

Moffett A. J., et al., 2016, MNRAS, 457, 1308

More S., van den Bosch F. C., Cacciato M., Mo H. J., Yang X., Li R., 2009, MNRAS, 392, 801

Muñoz-Cuartas J. C., Macciò A. V., Gottlöber S., Dutton A. A., 2011, MNRAS, 411, 584

Naab T., Johansson P. H., Ostriker J. P., 2009, ApJ, 699, L178

Navarro J. F., White S. D. M., 1993, MNRAS, 265, 271

Navarro J. F., Frenk C. S., White S. D. M., 1997, ApJ, 490, 493

Peebles P. J. E., 1969, ApJ, 155, 393

Peng C. Y., Ho L. C., Impey C. D., Rix H.-W., 2002, AJ, 124, 266

Peng C. Y., Ho L. C., Impey C. D., Rix H.-W., 2010, AJ, 139, 2097

Press W. H., Schechter P., 1974, ApJ, 187, 425

Rees M. J., Ostriker J. P., 1977, MNRAS, 179, 541

Schaye J., et al., 2015, MNRAS, 446, 521

Schmidt M., 1959, ApJ, 129, 243

Sérsic J. L., 1963, Boletin de la Asociacion Argentina de Astronomia La Plata Argentina, 6, 41

Sheth R. K., Mo H. J., Tormen G., 2001, MNRAS, 323, 1

Smith R., Choi H., Lee J., Rhee J., Sanchez-Janssen R., Yi S. K., 2016, ApJ, 833, 109

Somerville R. S., et al., 2008, ApJ, 672, 776

Tully R. B., Fisher J. R., 1977, A&A, 54, 661

Vale A., Ostriker J. P., 2006, MNRAS, 371, 1173

Velander M., Kuijken K., Schrabback T., 2011, MNRAS, 412, 2665

Velander M., et al., 2014, MNRAS, 437, 2111

Vogelsberger M., et al., 2014, MNRAS, 444, 1518

Wechsler R. H., Bullock J. S., Primack J. R., Kravtsov A. V., Dekel A., 2002, ApJ, 568, 52

White S. D. M., Rees M. J., 1978, MNRAS, 183, 341

Zu Y., Mandelbaum R., 2015, MNRAS, 454, 1161

de Vaucouleurs G., 1948, Annales d'Astrophysique, 11, 247

van Waerbeke L., 2000, MNRAS, 313, 524

van der Wel A., et al., 2014, ApJ, 788, 28

Appendix A

Comparison with AEGIS

The galaxy-by-galaxy comparison of the three main Sérsic parameters as a function of magnitude is shown in Figure A.1. The average scatter in the effective radius fits is 0.15 dex and does not change significantly over the magnitude range of interest. When the apparent sizes of CFHT galaxies are very small, they are impacted by atmospheric seeing, smearing them out and making them appear larger they are. This is seen in Figure A.2 comparing the apparent sizes of objects as determined by ACS and CFHT. The smallest galaxies marked in green show a consistent tendency to appear larger to CFHT, but they are misidentified as stars and prevented from inclusion in the lens stacks. The unflagged, correctly identified galaxies show no such offset, and so we can be confident that within our magnitude limits, we can accurately recover galaxy sizes via GALFIT.

As a final check to the quality of our size fits relative to AEGIS, we fit the M_*-$r_{\rm eff}$ relationship for the CFHT and ACS fits and compare. These

Table A.1: Power-law fits for the mass-size relationship of the AEGIS overlap galaxies.

Galaxy Sample	α	β
CFHT Blue	0.170 ± 0.009	-1.05 ± 0.08
ACS Blue	0.179 ± 0.009	-1.15 ± 0.09
CFHT Red	0.29 ± 0.02	-2.6 ± 0.2
ACS Red	0.29 ± 0.02	-2.6 ± 0.3

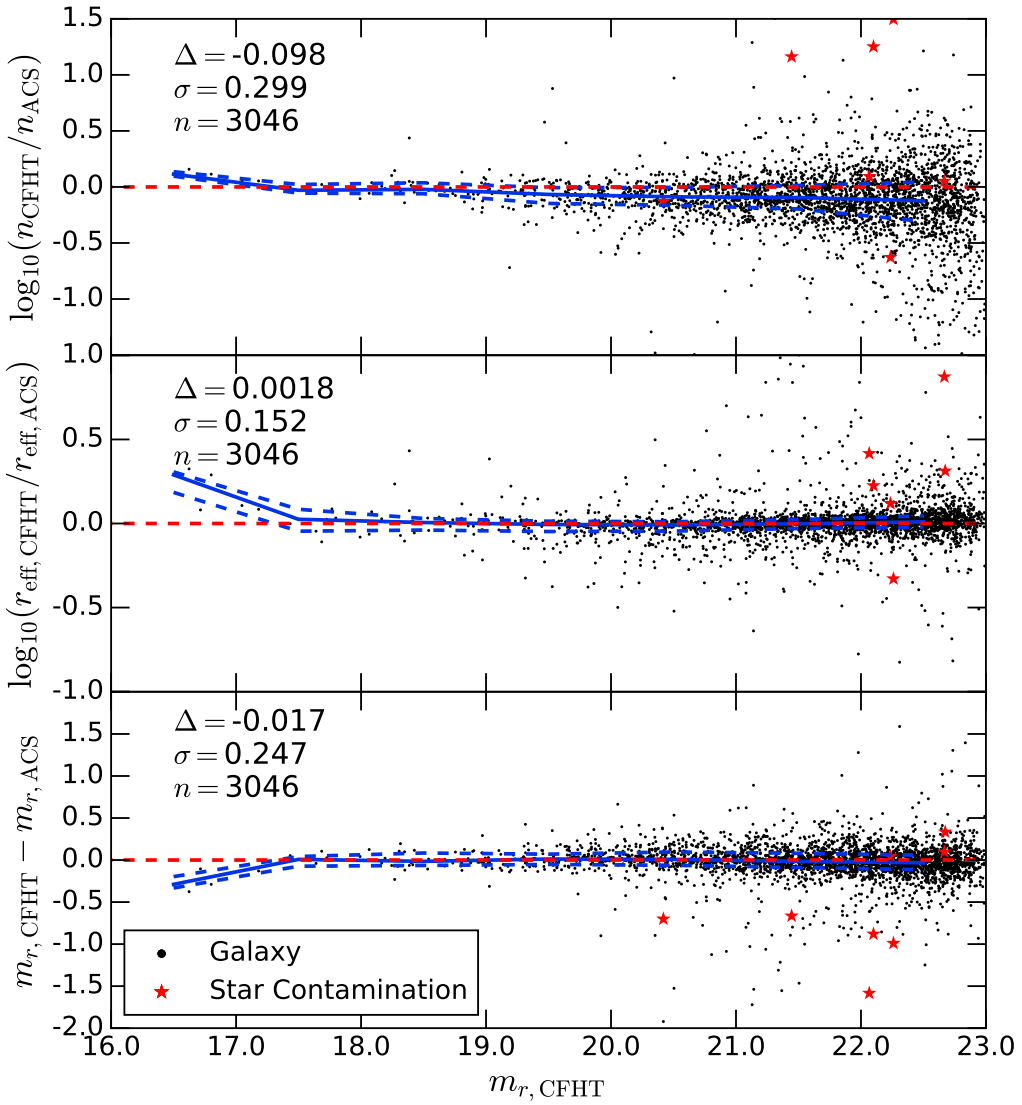

Figure A.1: Comparison of GALFITM results for galaxies in common to AEGIS and CFHTLenS. Black points are objects classified as galaxies by SExtractor in both surveys and red points are objects classified as stars in AEGIS which in CFHTLS are mis-classified as galaxies. The blue line is the median offset in each parameter, the dashed blue line indicates the semi-interquartile range.

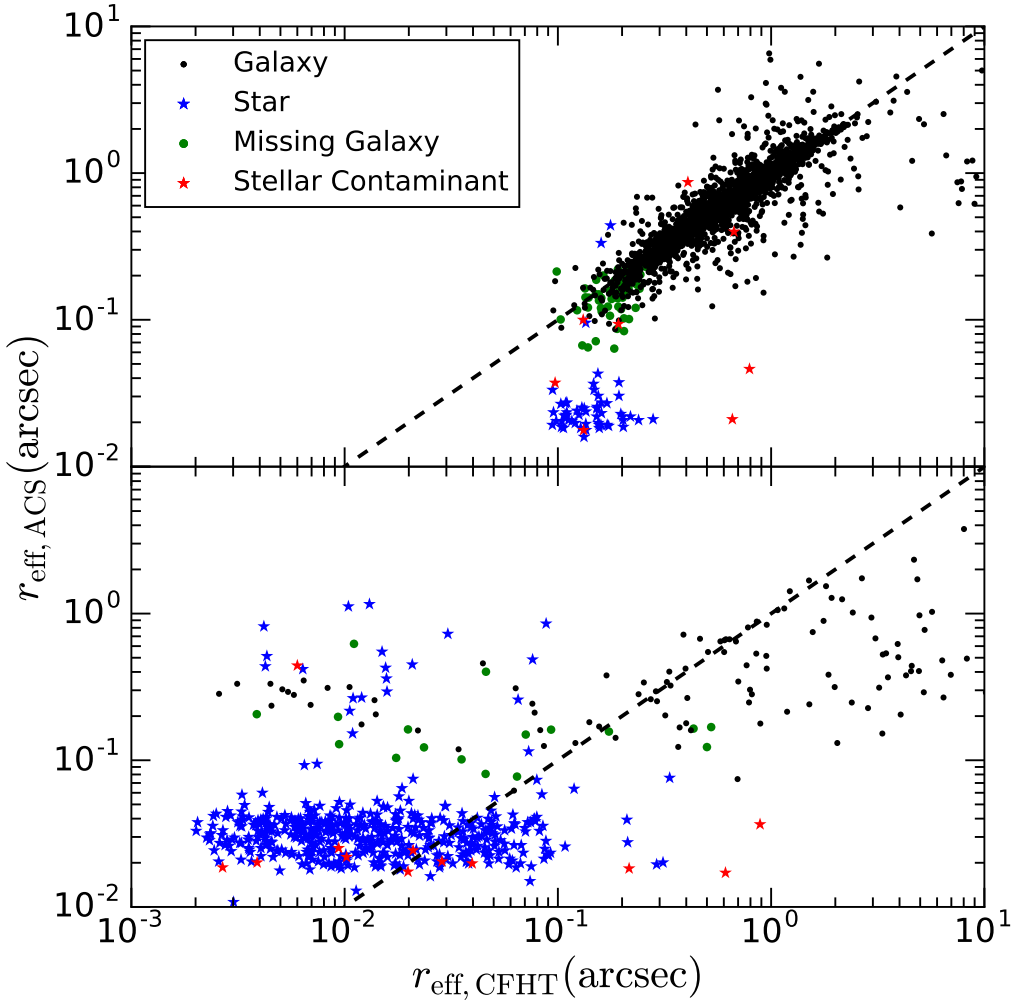

Figure A.2: Apparent size comparison of the objects in the AEGIS overlap. The left panel shows objects with unflagged model fits, the right panel shows objects with flagged model fits. Missing galaxies have been identified as galaxies in the higher resolution HST imaging, and identified as stars in the CFHT imaging, so they will not be included in our stacks. The stellar contamination is caused by stars that are misidentified as galaxies in the CFHTLenS catalogues. The unflagged objects show no systematic disagreements in apparent size at small radii, showing that GALFIT reliably models apparent size for galaxies which it can fit successfully.

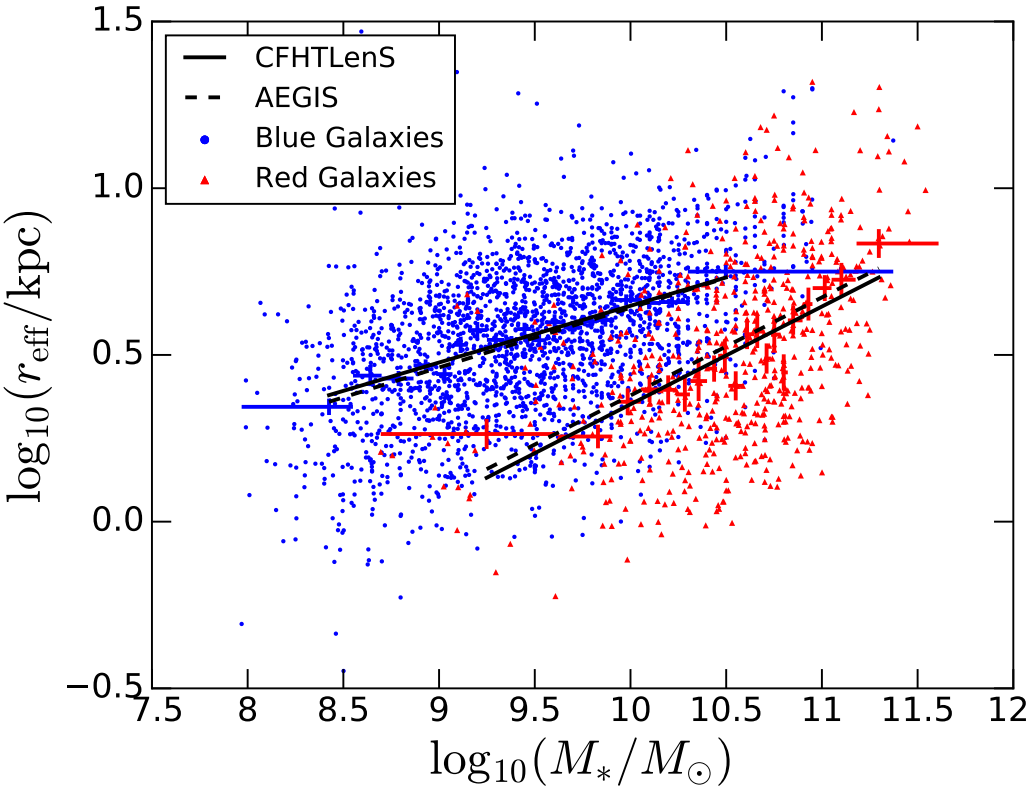

Figure A.3: Mass-Size relationship of EGS galaxies by CFHTLS. Points are size fits as determined by this work. Crosses represent the median mass and size of the galaxies in a each bin. The solid black lines are size-mass fits to the CFHTLenS data, the dashed lines are the fits to the AEGIS data.

fits are shown in Figure A.3. GALFIT's errors are generally understood to be underestimated (Häussler et al. 2007) so we avoid fitting the relationship using individual galaxies. We bin galaxies into groups of 120 for blue galaxies, and 30 for red galaxies, as there are roughly four times more blue galaxies in our sample. Next we fit a power law to the median $r_{\rm eff}$ of each bin as a function of M_* of the form

$$\log_{10}(r_{\rm eff,med}) = \alpha \cdot \log_{10}(M_{*,\rm med}) + \beta \tag{A.1}$$

$$r_{\rm eff,med} = M_{*,\rm med}^{\alpha} \cdot 10^{\beta} \tag{A.2}$$

The results of the fits are shown in table A.1, and we see no significant systematic difference between AEGIS fits and CFHT fits in the M_*-$r_{\rm eff}$ relationship. This indicates that while fits to individual galaxies may differ, no significant systematic differences are present that, on average, would result in an improper division of galaxies into our size bins.

Appendix B

Simulation Data

In this section we include the data from the EAGLE and Illustris simulations. Plots of individual galaxies (figures B.1 & B.2) show the differences between centrals and satellites leading to the differing η values we fit. Centrals consist of galaxies that the simulations flag as the most massive in their subhalo groups. This means that centrals can be field galaxies with a several (or zero) satellites, brightest group galaxies, or brightest cluster galaxies. In contrast, satellites are considered to be any galaxies besides the most massive member of the main subhalo group they reside in; i.e. the second most massive galaxy in a cluster is still considered a satellite even if it has its own satellites.

When we examine the halo mass-size plots in detail we see that both simulations are qualitatively similar. Central galaxies are more tightly clustered at higher masses and distinct from the broad swath of satellite galaxies at lower masses. For satellite galaxies, we see the same clustering of galaxies at intermediate sizes with a tail leading off at low mass and size. We also see that the three satellite galaxy bins tend toward smaller sizes, while the three central galaxy bins tend toward larger sizes. Despite overall differences in the halo-mass size relationship in both simulations, we see a consistency in the distribution of galaxies that allows us to use them as a meaningful point of comparison to our data.

Table B.1: Fit results for EAGLE galaxies.

Colour	N	f_{sat}	$\log_{10}(\langle M_{*,all}\rangle)$	η_{all}	$\log_{10}(\langle M_{*,cent}\rangle)$	η_{cent}	$\log_{10}(\langle M_{*,sub}\rangle)$	η_{sub}
Blue	4473	0.363	9.468	0.055 ± 0.045	9.469	-0.172 ± 0.033	9.466	0.60 ± 0.10
Blue	2620	0.366	9.976	0.275 ± 0.064	9.981	0.094 ± 0.062	9.966	0.57 ± 0.11
Blue	1276	0.290	10.439	0.51 ± 0.10	10.447	0.34 ± 0.10	10.420	0.68 ± 0.18
Blue	341	0.173	10.947	0.78 ± 0.18	10.959	0.55 ± 0.17	10.887	1.22 ± 0.40
Red	534	0.670	10.239	0.73 ± 0.23	10.281	0.39 ± 0.20	10.216	0.65 ± 0.29
Red	478	0.395	10.771	0.74 ± 0.11	10.811	0.400 ± 0.097	10.700	0.76 ± 0.27
Red	57	0.263	11.318	0.74 ± 0.32	11.341	0.29 ± 0.23	11.246	1.0 ± 1.0
Red	14	0.000	11.745	0.06 ± 0.34	11.745	0.06 ± 0.34	$--$	$--\pm--$

Table B.2: Fit results for Illustris galaxies.

Colour	N	f_{sat}	$\log_{10}(\langle M_{*,all} \rangle)$	η_{all}	$\log_{10}(\langle M_{*,cent} \rangle)$	η_{cent}	$\log_{10}(\langle M_{*,sub} \rangle)$	η_{sub}
Blue	11698	0.261	9.227	0.504 ± 0.033	9.212	0.213 ± 0.028	9.269	0.800 ± 0.078
Blue	5462	0.267	9.724	0.450 ± 0.048	9.711	0.030 ± 0.045	9.758	0.80 ± 0.11
Blue	2405	0.257	10.190	0.342 ± 0.067	10.182	-0.124 ± 0.066	10.212	0.99 ± 0.15
Blue	1202	0.250	10.681	0.567 ± 0.099	10.670	0.17 ± 0.10	10.710	1.05 ± 0.22
Red	207	0.831	10.015	0.11 ± 0.38	10.028	-0.45 ± 0.52	10.012	0.12 ± 0.34
Red	225	0.596	10.653	0.65 ± 0.33	10.683	-0.02 ± 0.25	10.631	0.77 ± 0.51
Red	117	0.359	11.038	0.78 ± 0.27	11.044	0.29 ± 0.22	11.028	1.06 ± 0.55
Red	105	0.276	11.331	0.58 ± 0.26	11.340	0.29 ± 0.24	11.307	-0.12 ± 0.94
Red	38	0.132	11.776	0.50 ± 0.31	11.792	0.40 ± 0.37	$--$	$--\pm--$

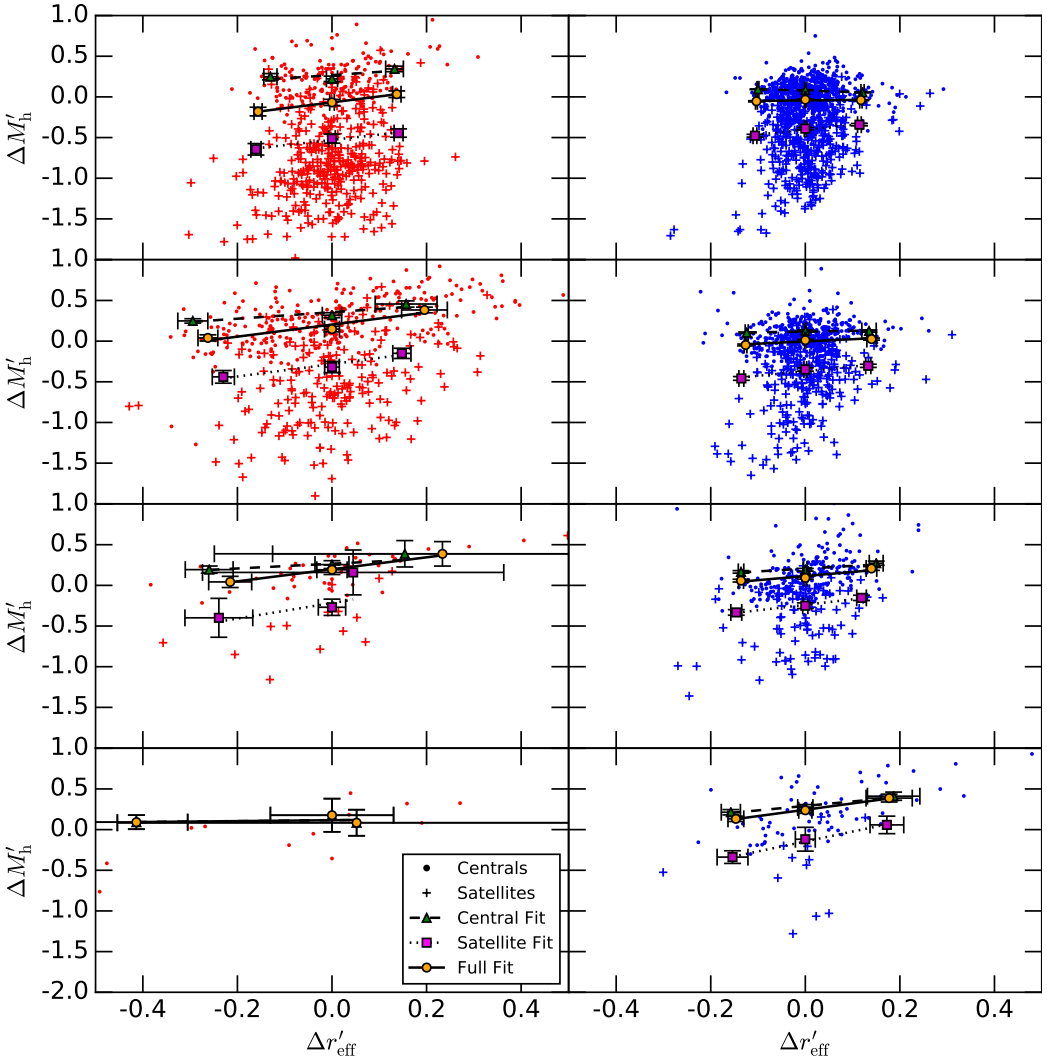

Figure B.1: Halo mass-size relationships for a sample of EAGLE galaxies colour coded as red/blue galaxies, with the stellar mass bin increasing from top to bottom. Circles are central galaxies, crosses are satellites. The green, magenta, and orange points (for centrals, satellites, and the full bin, respectively) are the averages and errors on the averages that we use to fit η. The dashed, dotted, and solid lines show the best fit slopes for η, for centrals, satellites, and the full bin.

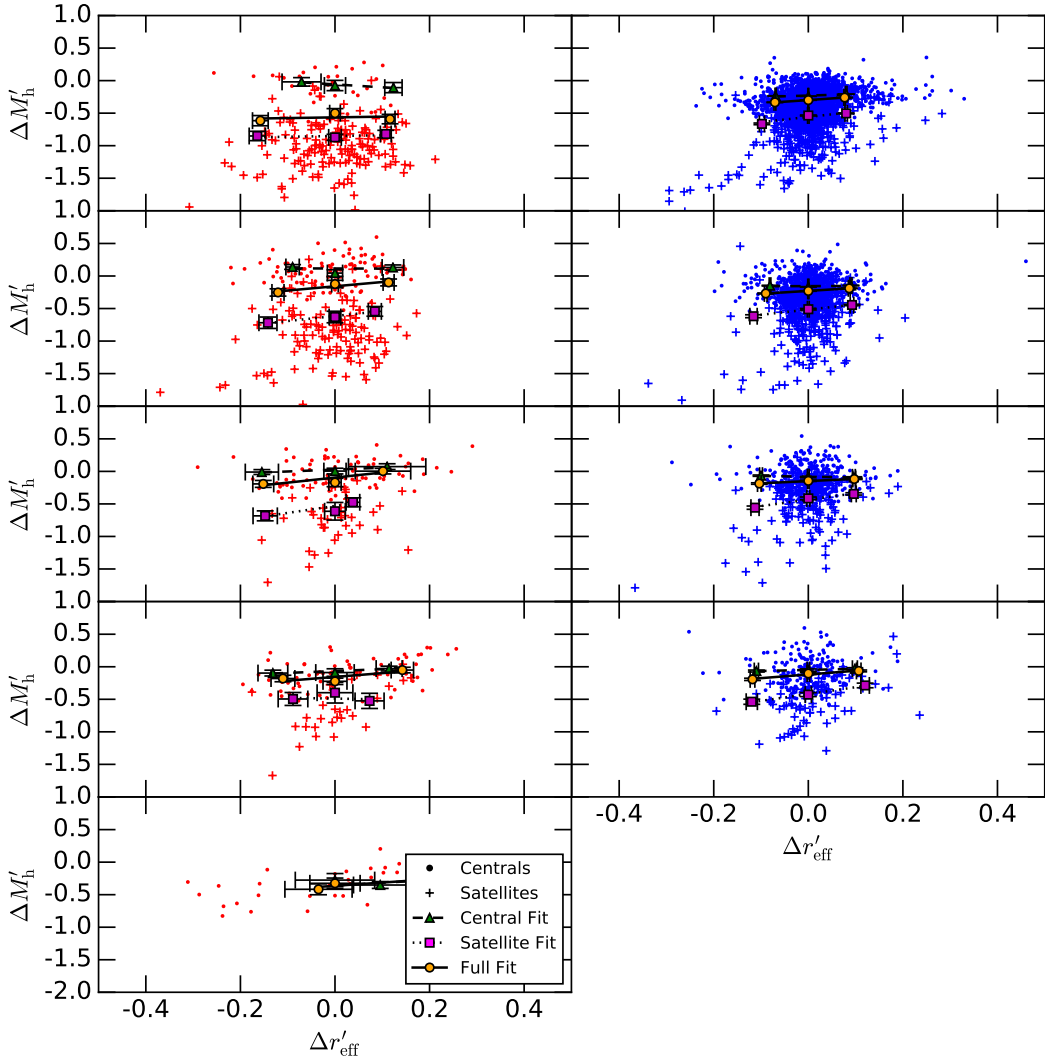

Figure B.2: Halo mass-size relationships for a sample of Illustris galaxies colour coded as red/blue galaxies, with the stellar mass bin increasing from top to bottom. Circles are central galaxies, crosses are satellites. The green, magenta, and orange points (for centrals, satellites, and the full bin, respectively) are the averages and errors on the averages that we use to fit η. The dashed, dotted, and solid lines show the best fit slopes for η, for centrals, satellites, and the full bin.